bioRxiv preprint doi: https://doi.org/10.1101/2023.01.31.526529; this version posted February 3, 2023. The copyright holder for this preprint (which was not certified by peer review) is the author/funder, who has granted bioRxiv a license to display the preprint in perpetuity. It is made available under aCC-BY-NC-ND 4.0 International license.

B3GALT6 Promotes Dormant Breast Cancer Cell Survival and Recurrence by Enabling Heparan Sulfate-Mediated FGF Signaling

Amulya Sreekumar[1,2], Michelle Lu[1,2], Biswa Choudhury[4], Tien-chi Pan[1,2], Dhruv K. Pant[1,2], Christopher J. Sterner[1,2], George K. Belka[1,2], Takashi Toriumi[1,2], Brian Benz[1,2], Matias Escobar-Aguirre[1,2], Francesco E. Marino[1,2], Jeffrey D. Esko[4], Lewis A. Chodosh[1,2,3 *]

[1]Department of Cancer Biology, [2]Abramson Family Cancer Research Institute, [3]Department of Medicine, Perelman School of Medicine at the University of Pennsylvania, PA 19104, USA. [4]Department of Cellular and Molecular Medicine, Glycobiology Research and Training Center, University of California, San Diego, La Jolla, CA 92093, USA.

Lead contact:
Lewis A. Chodosh, M.D., Ph.D., *Correspondence: chodosh@pennmedicine.upenn.edu
Room 614 BRB II/III, 421 Curie Boulevard, Philadelphia, PA 19104-6160, USA

bioRxiv preprint doi: https://doi.org/10.1101/2023.01.31.526529; this version posted February 3, 2023. The copyright holder for this preprint (which was not certified by peer review) is the author/funder, who has granted bioRxiv a license to display the preprint in perpetuity. It is made available under aCC-BY-NC-ND 4.0 International license.

Summary

Breast cancer mortality results primarily from incurable recurrent tumors seeded by dormant, therapy-refractory residual tumor cells (RTCs). Understanding the mechanisms enabling dormant RTC survival is therefore essential for improving patient outcomes. We derived a dormancy-associated RTC signature that mirrors the transcriptional response to neoadjuvant chemotherapy in patients and is enriched for extracellular matrix-related pathways. In vivo CRISPR-Cas9 screening of dormancy-associated candidate genes identified the galactosyltransferase B3GALT6 as a functional regulator of RTC fitness. B3GALT6 covalently attaches glycosaminoglycans (GAGs) to proteins to generate proteoglycans and its germline loss-of-function causes skeletal dysplasias. We determined that B3GALT6-mediated biosynthesis of the GAG heparan sulfate predicts poor patient outcomes, promotes tumor recurrence by enhancing dormant RTC survival in multiple contexts, and does so via a B3GALT6-heparan sulfate/HS6ST1-heparan 6-*O*-sulfation/FGF1-FGFR2 signaling axis. These findings identify a role for B3GALT6 in cancer and suggest targeting FGF signaling as a novel approach to preventing recurrence by eradicating dormant RTCs.

Keywords: B3GALT6, dormancy, breast cancer, proteoglycans, glycosaminoglycans, glycans, heparan sulfate, HS6ST1, 6-*O*-sulfation, FGF

bioRxiv preprint doi: https://doi.org/10.1101/2023.01.31.526529; this version posted February 3, 2023. The copyright holder for this preprint (which was not certified by peer review) is the author/funder, who has granted bioRxiv a license to display the preprint in perpetuity. It is made available under aCC-BY-NC-ND 4.0 International license.

Introduction

Despite advances in early detection and treatment, breast cancer remains the leading cause of cancer-related deaths among women worldwide[1]. Mortality results predominantly from incurable recurrences that arise years, or even decades, following treatment of the primary tumor (PT)[2,3]. Since recurrent tumors derive from residual tumor cells (RTCs) that survive therapy, and are believed to reside in a reversibly quiescent, non-proliferative state of cellular dormancy[4], depleting this critical pool of cells by targeting their survival mechanisms represents an attractive approach to preventing breast cancer recurrence.

RTC dormancy can be selected for or induced by exposure to therapy and/or interaction with a foreign microenvironment following cancer cell dissemination from the primary site. Experimental models recapitulating these paradigms of dormancy induction have been used to identify mechanisms underlying RTC persistence and recurrence. These include i) therapy-associated models that mimic RTC survival following targeted therapy by downregulating oncogenes such as *Her2*[5,6], *Wnt1*[6,7], and *Fgfr1*[8], and ii) models that recapitulate interactions between RTCs and a foreign microenvironment, such as the D2.OR/D2A1 paired cell line model[9-11].

Recent data suggest marked overlap of dormant RTC gene expression profiles that may be independent of both the location of RTCs at primary or metastatic sites and the stimulus responsible for dormancy entry[6,12]. Consequently, investigating conserved elements of dormancy-associated gene expression signatures may provide a tractable approach for identifying unique dependencies of dormant RTCs that could be targeted to induce their elimination, thereby preventing recurrence. Among these dependencies, crosstalk between RTCs and components of the extracellular matrix (ECM), including thrombospondin[13], laminins[14,15], fibronectin[16-19], and collagens[20-22], have been reported to promote RTC survival and dormancy. In contrast, little is known about the role of other ECM components, including proteoglycans, in regulating dormancy and RTC fitness.

bioRxiv preprint doi: https://doi.org/10.1101/2023.01.31.526529; this version posted February 3, 2023. The copyright holder for this preprint (which was not certified by peer review) is the author/funder, who has granted bioRxiv a license to display the preprint in perpetuity. It is made available under aCC-BY-NC-ND 4.0 International license.

Proteoglycans consist of unique core proteins covalently linked to one or more glycosaminoglycan (GAG) side chains[23], and are subclassified as heparan sulfate, chondroitin/dermatan sulfate, or keratan sulfate proteoglycans based on the type of GAG they contain[24]. Following their assembly, proteoglycans can be embedded into the plasma membrane, secreted from the cell, or shed into the ECM where they orchestrate a variety of biological activities[25,26].

A defining feature of GAGs that underlies their biological function is their highly anionic nature[23], which is imparted by their component uronic acid residues and by dynamic, spatially regulated sulfation[27]. Anionic GAGs avidly bind growth factors, thereby regulating cellular signaling as well as phenotypes such as proliferation and survival[23]. The impact of these modified glycans on RTC fitness and breast cancer progression is unknown.

Here, we performed an in vivo CRISPR-Cas9 screen targeting a core set of dormancy-associated, tumor cell-autonomous genes to identify functional regulators of dormant RTC survival. The strongest hit from this screen was *B3galt6*, a galactosyltransferase that is essential for proteoglycan assembly[28] and whose germline loss-of-function gives rise to the connective tissue disorders spondyloepimetaphyseal dysplasia with joint laxity, type 1 (SEMD-JL1), spondylodysplastic Ehlers-Danlos syndrome (spEDS), and Al-Gazali syndrome[29-31]. A role for B3GALT6 in cancer has not been reported. Our studies identify proteoglycan synthesis as a critical vulnerability of dormant RTC fitness that promotes their survival and recurrence, in part through B3GALT6-enabled heparan sulfate proteoglycan synthesis that potentiates FGF signaling in RTCs. Our observations indicate that RTC survival is dependent upon tumor cell-autonomous heparan sulfate synthesis and FGF signaling, which may constitute a targetable node to prevent lethal breast cancer recurrences.

Results

bioRxiv preprint doi: https://doi.org/10.1101/2023.01.31.526529; this version posted February 3, 2023. The copyright holder for this preprint (which was not certified by peer review) is the author/funder, who has granted bioRxiv a license to display the preprint in perpetuity. It is made available under aCC-BY-NC-ND 4.0 International license.

Dormant tumor cells display cell-autonomous upregulation of ECM-related transcripts following therapy

To understand the mechanisms underlying dormant RTC survival and persistence, we have developed and characterized doxycycline-inducible genetically engineered mouse (GEM) models of breast cancer[5-7,32-37]. These models of cellular dormancy[6] enable robust spatiotemporal regulation of oncogene activation, thereby modeling the effects of targeted therapy in patients and permitting study of the impact of oncogenic pathway inhibition in genetically complex PTs, as well as the contribution of dormant RTCs to spontaneous recurrence.

RTCs that survive PT regression induced by Her2 downregulation in *MMTV-rtTA;TetO-Her2/neu* (*MTB/TAN*) mice[5], or by Wnt1 downregulation in *MMTV-rtTA;TetO-Wnt1* (*MTB/TWNT*) mice[7], were previously isolated to generate RTC-specific gene expression signatures[6]. Dormancy signatures from *MTB/TAN* and *MTB/TWNT* mice were highly concordant, suggesting conserved elements of the dormant state[6].

Dormancy-associated changes in gene expression in RTCs in vivo in the context of therapy could be imposed by the microenvironment or could result from cell-autonomous determinants. To identify a core set of tumor cell-autonomous regulators of RTC survival and dormancy, we cultured PT cells (PTCs) from the Her2-dependent model in vitro (**Fig. 1A**). Maintaining Her2-dependent tumor cells in the presence of doxycycline under reduced serum conditions resulted in high levels of Her2 expression and proliferation as measured by Ki67 and EdU (D0; *baseline*) (**Fig. 1B, C**). Withdrawing doxycycline elicited the rapid decay of Her2 levels (Her2 *deinduction*) and cellular proliferation, with negligible levels of Ki67 and EdU detected at 7, 14, and 28 days post-doxycycline withdrawal (D7, D14, D28). Importantly, re-addition of doxycycline to quiescent tumor cells (Her2 *reinduction*) at each of these time points rapidly restored Her2 levels and proliferation to baseline levels (D7+, D14+, D28+) (**Fig. 1B, C**). Thus,

bioRxiv preprint doi: https://doi.org/10.1101/2023.01.31.526529; this version posted February 3, 2023. The copyright holder for this preprint (which was not certified by peer review) is the author/funder, who has granted bioRxiv a license to display the preprint in perpetuity. It is made available under aCC-BY-NC-ND 4.0 International license.

the quiescent state of these cells is reversible, which is a *sine qua non* of cellular dormancy, confirming that this in vitro system recapitulates key features of dormancy observed in vivo[6,32,38].

To identify a core set of dormancy-associated genes, we performed RNA-sequencing on cells in vitro at *baseline*, *deinduction*, and *reinduction* time points. We evaluated whether dormancy-associated gene expression changes are conserved in dormant *MTB/TAN* and *MTB/TWNT* RTCs in vivo (PTCs vs. D28 RTCs) and *MTB/TAN* cells in vitro (D0 vs. D28) and found extensive overlap in the set of downregulated genes between these models (p=6.87e-21) (**Fig. S1A**). As anticipated, gene ontology analysis of the overlapping set of 747 downregulated genes identified enrichment for pathways related to cell cycle, cellular biosynthesis, and translation (**Fig. S1B**).

Conversely, we found a highly significant overlap among genes upregulated during dormancy in vivo (PTCs vs. D28 RTCs) and in vitro (D0 vs. D28) (540 genes, p=1.63e-15) (**Fig. 1D**). Intriguingly, gene ontology analysis of this overlapping gene set identified enrichment for multiple pathways related to the organization and metabolism of ECM components (**Fig. 1E**). We refer to the overlapping in vivo and in vitro-derived up- and down-regulated gene sets as the core RTC signature.

Thus, by integrating dormancy-associated gene expression changes that occur in vitro and in vivo, we generated a therapy-associated core RTC signature that is enriched for conserved features of the dormant state, including the tumor cell-autonomous synthesis of ECM components.

A core RTC dormancy signature recapitulates neoadjuvant chemotherapy-associated gene expression changes and predicts favorable outcomes in patients

To evaluate whether the core RTC signature exhibited by dormant tumor cells following Her2 downregulation is clinically relevant, we interrogated data from six publicly available datasets comprised of paired gene expression profiles for primary breast cancers and residual

bioRxiv preprint doi: https://doi.org/10.1101/2023.01.31.526529; this version posted February 3, 2023. The copyright holder for this preprint (which was not certified by peer review) is the author/funder, who has granted bioRxiv a license to display the preprint in perpetuity. It is made available under aCC-BY-NC-ND 4.0 International license.

tumors in patients that were first biopsied and then surgically resected following neoadjuvant chemotherapy[39-45]. Five of these six datasets displayed significant enrichment for the core RTC signature post-therapy (**Fig. 1F**), even after excluding proliferation-associated genes (**Fig. S1C**). Notably, enrichment for this signature was independent of both the type (chemotherapy or endocrine therapy) and duration of therapy. These findings indicate that mouse dormancy models recapitulate clinically-relevant aspects of the response of breast cancers to therapy in patients and suggest that therapy-refractory tumor cells that persist in patients exhibit changes in gene expression that are similar to those associated with cellular dormancy in mice.

To evaluate the prognostic power of the core RTC signature in breast cancer patients, we performed a meta-analysis of patient-derived recurrence data. Analogous to prior observations for an in vivo *MTB/TAN* and *MTB/TWNT*-derived RTC dormancy signature[6], we found that patients whose PTs were enriched for the core RTC signature exhibited a striking decrease in risk of recurrence (HR=0.14; p=1.1e-29), ostensibly reflecting a higher propensity of such tumors to display indolent properties (**Fig. S1D**). This association was substantially stronger for the core RTC signature (HR=0.14) vs. the in vivo signature alone (HR=0.49)[6], and persisted following the removal of proliferation-associated genes (p=3.2e-18), indicating that the core signature reflects features of cellular dormancy beyond those related to cell cycle-arrest (**Fig. S1E**). Furthermore, since >75% of patient tumors in this dataset were estrogen receptor positive (ER+) and displayed metastatic recurrence, our findings suggest that a conserved RTC signature generated from ER-negative RTCs at local sites can inform the study of mechanisms enabling RTC survival and persistence in the contexts of both distant recurrence and ER+ disease[6].

In conclusion, we found enrichment of a core RTC signature in residual lesions from patients treated with different neoadjuvant chemotherapies, and determined that this signature is significantly associated with risk of tumor recurrence in patients across multiple breast cancer subtypes, and at both local and distant sites of recurrence.

bioRxiv preprint doi: https://doi.org/10.1101/2023.01.31.526529; this version posted February 3, 2023. The copyright holder for this preprint (which was not certified by peer review) is the author/funder, who has granted bioRxiv a license to display the preprint in perpetuity. It is made available under aCC-BY-NC-ND 4.0 International license.

An in vivo ECM-focused loss-of-function screen identifies *B3galt6* as a regulator of RTC fitness

Having derived a core RTC signature, we reasoned that genes upregulated during dormancy in a manner that is reversible following Her2 reinduction might be involved in promoting RTC dormancy and/or survival. To test this hypothesis, we focused on a clustered set of genes enriched for ECM-associated gene ontology terms that displayed a similar temporal pattern of upregulation during in vitro dormancy (IVD) that was reversed upon Her2 reinduction (**Fig. 2A**).

To determine whether genes within this cluster might functionally regulate RTC survival in a tumor cell-intrinsic manner, we performed an in vivo CRISPR-Cas9-based loss-of-function screen. We designed a custom sgRNA library with 4-5 sgRNAs targeting each of 95 candidate genes that displayed strong, dormancy-selective expression and were enriched within ECM-associated ontology terms (**Table S1**). An additional 53 sgRNAs comprising positive controls anticipated to be lethal to proliferative cells (*e.g.*, sg*Rpa3*, sg*Pcna*) and negative controls consisting of non-targeting sgRNAs and sgRNAs targeting inert sites (*e.g.*, sg*Rosa*) anticipated to lack selection during tumor dormancy and recurrence (**Fig. 2B, Table S1**).

MTB/TAN-derived Her2-dependent PTCs constitutively expressing Cas9 (Her2-dependent-Cas9 cells) were transduced with this GFP-labeled sgRNA library at low multiplicity of infection (MOI=0.3) and sorted to ensure that each cell contained a single sgRNA. After confirming that all sgRNAs were represented within GFP+ sorted cells (**Fig. S2A**), cells were orthotopically injected into nude (*nu/nu*) mice. To assess sgRNA selection during disease progression, we allowed Her2-driven PTs to form in the presence of doxycycline, then withdrew doxycycline to induce tumor regression to a non-palpable, dormant state (**Fig. S2B)**. PTs and residual lesions (RLs) were harvested at time points corresponding to early (D7), mid (D14) and

bioRxiv preprint doi: https://doi.org/10.1101/2023.01.31.526529; this version posted February 3, 2023. The copyright holder for this preprint (which was not certified by peer review) is the author/funder, who has granted bioRxiv a license to display the preprint in perpetuity. It is made available under aCC-BY-NC-ND 4.0 International license.

late (D28, D35) dormancy following tumor regression to assess sgRNA composition at each stage of tumor progression (**Fig. 2B**).

By sequencing the initial plasmid pool, sorted cells, injected cells, PT and RL samples, we confirmed that all sgRNAs were detectable at each time point (**Fig. S2A**). Calculating the Gini index to quantify the skewness of sgRNA distribution revealed that the plasmid pool, sorted cells, and injected cells displayed low Gini indices (median=0.21, 0.25, and 0.26, respectively), confirming that the distribution of sgRNAs remained relatively homogeneous at these points. PTs displayed a slightly higher Gini index than pre-injection samples (median=0.29), suggesting only modest selection of sgRNAs in the presence of the strong oncogenic driver, Her2. In contrast, RLs displayed substantial stepwise increases in Gini indices at D7, D14, D28, and D35 (median=0.38, 0.45, 0.58, 0.69, respectively), confirming that sgRNAs were progressively selected throughout the dormancy period (**Fig. 2C**).

To identify sgRNAs that underwent selection, we employed 8 analytical methods and ranked sgRNAs identified by 2 or more methods. Consistent with our prior findings that RTCs in this model are non-proliferative following Her2 downregulation[6], sg*Rpa3* and sg*Pcna* positive controls were depleted during PT formation (**Fig. S2C**), but not following Her2 downregulation (**Fig. S2D**).

We reasoned that sgRNAs targeting genes that maintain cell cycle-arrest following Her2 down-regulation would be enriched in RLs vs. PTs. Our finding that *Ddr1,* a known regulator of cell cycle arrest[22], is enriched in this manner lends credence to this hypothesis (**Fig. S2E**). Conversely, we anticipated that sgRNAs targeting genes that promote cell survival following Her2 down-regulation would be depleted in RLs vs. PTs, as supported by the identification of the pro-survival gene, *Bcl2*, as one of two top hits in this analysis (**Fig. 2D**).

The second top putative pro-survival hit identified by all 8 methods in each of four pairwise comparisons of PT and RL time points was *B3galt6* (**Fig. 2D, S2F**). Analyzing the distribution of sgRNAs targeting *B3galt6* (colored bars) vs. all sgRNAs (grey histogram) in each

bioRxiv preprint doi: https://doi.org/10.1101/2023.01.31.526529; this version posted February 3, 2023. The copyright holder for this preprint (which was not certified by peer review) is the author/funder, who has granted bioRxiv a license to display the preprint in perpetuity. It is made available under aCC-BY-NC-ND 4.0 International license.

pairwise comparison confirmed that *B3galt6* sgRNAs were strongly depleted within 7 days following Her2 downregulation (PT vs. D7, D14) (**Fig. 2E, S2F**). Notably, *B3galt6* sgRNAs exhibited further depletion at later dormancy time points, as revealed by comparisons of early (D7) to later (D14, D28, D35) RL time points (**Fig. 2E, S2F**). This strong, persistent negative selection against cells harboring *B3galt6* sgRNAs suggests a potential role for B3GALT6 in dormancy.

B3GALT6 promotes RTC survival following therapy-associated dormancy

Beta-1,3-galactosyltransferase (B3GALT6) catalyzes the addition of the second Gal residue in the GlcA-Gal-Gal-Xyl-*O*- tetrasaccharide linker that is essential for the attachment of sulfated GAGs to proteoglycan core proteins[28]. Accordingly, B3GALT6 enzymatic activity is required for proteoglycan assembly. Based on their linear chains of repeating disaccharides, GAGs can be classified as: (i) heparan sulfate (GlcNAc-GlcA or GlcNAc-iduronic acid (IdoA)); (ii) chondroitin sulfate (GalNAc-GlcA); or (iii) dermatan sulfate (resulting from the epimerization of at least one GalNAc-GlcA to GalNAc-IdoA) (**Fig. 3A**). Consequently, deletion of the *B3galt6* gene using CRISPR-Cas9 should ablate both heparan and chondroitin/dermatan sulfate GAGs on cell surfaces[46].

To test this, we transduced Her2-dependent-Cas9 cells with sg*Rosa* or sg*B3galt6* vectors expressing GFP, performed ICE analysis[47], and confirmed that sg*B3galt6* efficiently induced indels predicted to result in loss-of-function mutations in >85% of tumor cells (**Fig. S3A, B**). Immunofluorescence performed on sg*Rosa* and sg*B3galt6* cells using a heparan sulfate antibody demonstrated a marked reduction in heparan sulfate levels in sg*B3galt6* cells vs. sg*Rosa* controls, providing further confirmation that these sgRNAs functionally reduce B3GALT6 activity (**Fig. 3B**).

To independently validate findings from our CRISPR-Cas9 screen, an in vitro competition assay was performed in which sg*Rosa*-GFP and sg*B3galt6*-GFP transduced Her2-

bioRxiv preprint doi: https://doi.org/10.1101/2023.01.31.526529; this version posted February 3, 2023. The copyright holder for this preprint (which was not certified by peer review) is the author/funder, who has granted bioRxiv a license to display the preprint in perpetuity. It is made available under aCC-BY-NC-ND 4.0 International license.

dependent-Cas9 cells were plated at a 1:1 ratio with sg*Rosa*-mCherry cells on D-3. Genomic DNA was harvested from cells at D-2 or D0 (*baseline*) in the presence of doxycycline, at D3, D7, D14, D21, and D28 following doxycycline withdrawal (*deinduction*), and at 48 hr after doxycycline re-addition to D28 deinduction cells (D28+, *reinduction*). Changes in the percentage of sg*B3galt6*-GFP:sg*Rosa*-mCherry cells relative to sg*Rosa*-GFP:sg*Rosa*-mCherry controls were quantified by droplet digital PCR (ddPCR) (**Fig. 3C**). Tumor cells expressing sg*B3galt6* were significantly and progressively depleted (p<0.0001) throughout dormancy beginning as early as 3 days following Her2 downregulation (**Fig. 3D**). These data indicate that B3GALT6 loss impairs RTC fitness in a tumor cell-autonomous manner.

To confirm that this dormancy-selective depletion of sg*B3galt6* cells also occurs in vivo, as predicted by our CRISPR-Cas9 screen, we performed a competition assay analogous to that performed in vitro. sg*Rosa*-mCherry Her2-dependent-Cas9 cells admixed with an equal number of sg*Rosa*-GFP or sg*B3galt6*-GFP cells were injected into mice maintained on doxycycline, following which PT (*baseline*) as well as RL samples at D10 (*early*) and D28 (*late*) following doxycycline withdrawal were harvested (**Fig. 3E**).

Samples were imaged using a stereoscope prior to processing for genomic DNA isolation and ddPCR. While no differences in GFP intensity were visible in PT samples across groups, decreases in GFP intensity for each of the sg*B3galt6* guides vs. sg*Rosa* controls were clearly evident in D10 and D28 RL samples (**Fig. 3E**). Consistent with this, ddPCR analysis confirmed pronounced negative selection against sg*B3galt6* tumor cells (p<0.0001) at D10 and D28 RL time points, as well as ongoing depletion from D10 to D28 (**Fig. 3F**). In contrast, sg*Rosa*-GFP cells showed no selection across time points. These data provide further evidence that B3GALT6 is required for maintaining RTC fitness in vivo.

To determine the cellular mechanisms by which B3GALT6 regulates RTC fitness in vivo, sg*B3galt6*_3-GFP or sg*Rosa*-GFP cells were injected into mice maintained on doxycycline, followed by harvest of PTs as well as early (D4, D7) RLs following doxycycline withdrawal. Mice

bioRxiv preprint doi: https://doi.org/10.1101/2023.01.31.526529; this version posted February 3, 2023. The copyright holder for this preprint (which was not certified by peer review) is the author/funder, who has granted bioRxiv a license to display the preprint in perpetuity. It is made available under aCC-BY-NC-ND 4.0 International license.

were injected with EdU 2 hr prior to sacrifice. As anticipated, a dramatic decrease in cell proliferation was observed in control lesions D4 and D7 following doxycycline withdrawal, as revealed by visualizing incorporation of the S-phase marker EdU (**Fig. 3G, H**) and immunofluorescence for the cell cycle marker Ki67 (**Fig. S3C, D**). No differences were observed in the percentage of EdU+ or Ki67+ RTCs between sg*B3galt6* and sg*Rosa*-derived PTs or D4 or D7 RLs (**Figs. 3G, H; S3C, D**). These findings confirm that RTCs in both sg*Rosa* and sg*B3galt6* groups enter a quiescent state following Her2 downregulation, and that the observed depletion of sg*B3galt6* RTCs vs. control cells following Her2 downregulation is unlikely to result from B3GALT6-dependent differences in proliferation.

Next, we asked if the decrease in sg*B3galt6* vs. *sgRosa* RTCs following Her2 downregulation is a consequence of differential cell survival by quantifying apoptotic cells by terminal deoxynucleotidyl transferase dUTP nick end labeling (TUNEL) (**Fig. 3I, J**), and by immunofluorescence for cleaved caspase 3, (cc3) (**Fig. S3E, F**). While no differences were evident in the percentage of TUNEL+ or cc3+ in PTs or D4 RLs between sg*B3galt6* and *sgRosa* samples, a significant increase in the percentage of TUNEL+ (p=0.0009) and cc3+ tumor cells (p=0.033) was apparent at D7 in sg*B3galt6* cells vs. sg*Rosa* RL samples. Together, these data indicate that the impaired fitness observed in sg*B3galt6* tumor cells following Her2 downregulation is attributable to higher levels of apoptosis in dormant sg*B3galt6* RTCs.

B3GALT6 promotes tumor recurrence following therapy-associated dormancy

In light of our observation that B3GALT6 promotes RTC fitness, we wished to determine whether this would impact the kinetics of spontaneous tumor recurrence. Her2-dependent-Cas9 cells transduced with sg*B3galt6*-GFP or sg*Rosa*-GFP at a target MOI=5 (**Fig. S4A, B**) were orthotopically injected into mice maintained on doxycycline to drive PT formation (**Fig. 4A**). sg*B3galt6* and sg*Rosa*-GFP groups displayed no differences in PT formation (p=0.26) (**Fig. S4C**).

bioRxiv preprint doi: https://doi.org/10.1101/2023.01.31.526529; this version posted February 3, 2023. The copyright holder for this preprint (which was not certified by peer review) is the author/funder, who has granted bioRxiv a license to display the preprint in perpetuity. It is made available under aCC-BY-NC-ND 4.0 International license.

Following doxycycline withdrawal to induce tumor regression to a non-palpable, dormant state, mice were monitored for tumor recurrence. Strikingly, dormant RLs derived from sg*B3galt6*_3 (p<0.0001; HR=0.13) or sg*B3galt6*_1 (p<0.0001; HR=0.11) tumor cells displayed dramatically delayed median recurrence-free survival vs. sg*Rosa* controls (**Fig. 4B**). Moreover, whereas all 20 recurrent tumors in the sg*Rosa* control group were strongly GFP+, only 1/20 sg*B3galt6*_3 and 3/20 sg*B3galt6*_1 recurrent tumors were GFP+ (**Fig. 4C**, **S4D**). This strong negative selection against sg*B3galt6* GFP+ cells in recurrences was confirmed by ddPCR, which demonstrated >10-fold depletion of GFP+ cells in sg*B3galt6*_3 (p=0.0003) and sg*B3galt6*_1 (p=0.039) recurrences (**Fig. 4D**). Together, the marked delay in spontaneous tumor recurrence observed for sg*B3galt6*- cells, coupled with the observation that the small fraction (~10%) of untransduced GFP-negative cells present efficiently and reproducibly outcompeted GFP+ sg*B3galt6* tumor cells during recurrent tumor formation, indicate that B3GALT6 is required for tumor recurrence.

To ensure that recurrences maintained B3GALT6 deletion (*i.e.*, remain GFP+), we transduced Her2-dependent-Cas9 cells with sg*Rosa*-GFP or sg*B3galt6*-GFP at a higher target MOI of 10 (**Fig. 4E**), which resulted in a transduction efficiency of >95% (**Fig. S4E, F**). Under these conditions, sg*B3galt6*-GFP cells exhibited a dramatic delay in median recurrence-free survival (135d) vs. sg*Rosa*-GFP (39.5d) cells (p<0.0001; HR=0.16) (**Fig. 4F**) that was even greater than that observed for cells transduced at lower MOI (86-91d vs. 51d) (**Fig. 4B**). Consistent with the higher MOI employed, nearly all recurrences arising from sg*B3galt6*-GFP (12/14) or sg*Rosa*-GFP (18/19) cells displayed strong GFP-positivity (**Fig. 4G, S4G**) and ddPCR confirmed that the number of GFP+ cells in sg*Rosa* and sg*B3galt6* recurrences was comparable (**Fig. 4H**). Further, immunofluorescence on recurrent tumor tissue confirmed that heparan sulfate levels were decreased in sg*B3galt6* vs. sg*Rosa* recurrences, as anticipated, thereby confirming that loss of B3GALT6 function was maintained in sg*B3galt6* recurrences (**Fig. S4H**).

bioRxiv preprint doi: https://doi.org/10.1101/2023.01.31.526529; this version posted February 3, 2023. The copyright holder for this preprint (which was not certified by peer review) is the author/funder, who has granted bioRxiv a license to display the preprint in perpetuity. It is made available under aCC-BY-NC-ND 4.0 International license.

These observations suggest that transducing tumor cells with sg*B3galt6* at high MOI eliminated a bypass pathway in which untransduced (*i.e.*, GFP-negative) cells give rise to recurrence.

EdU labeling failed to identify differences in proliferation between sg*Rosa* and sg*B3galt6* recurrences (**Fig. 4I, J**). In contrast, TUNEL staining revealed an increase in apoptotic tumor cells in sg*B3galt6* vs. sg*Rosa* recurrent tumors (p=0.018) (**Fig. 4K, L**). Consistent with these findings, a trending, albeit non-significant, decreased growth rate was observed for sg*B3galt6* vs. sg*Rosa* recurrences (p=0.073) (**Fig. 4M**). Together, these findings indicate that B3GALT6 is required for efficient tumor recurrence from dormant residual disease post-therapy.

B3GALT6 promotes tumor cell survival and outgrowth in microenvironment-induced dormancy

Our data to this point identified B3GALT6 as a critical regulator of RTC survival and recurrence in the context of therapy-associated dormancy. We next asked whether B3GALT6 might also play a functional role in microenvironment-induced dormancy. To address this question we used the D2.OR-D2A1 system of paired cell lines that share a common origin and grow comparably in two-dimensional (2D) culture, but manifest divergent growth properties (*i.e.*, D2.OR: dormant/indolent vs. D2A1: proliferative/aggressive) when cultured in 3D or at metastatic sites in vivo[16,20,48].

We first determined whether a previously derived dormancy-associated gene expression signature generated by comparing D2.OR to D2A1 cells grown in 3D culture[48] exhibited overlap with dormancy-associated gene expression changes in *MTB/TAN* cells following Her2 downregulation in vitro and in vivo. Gene expression changes observed in Her2-dependent tumor cells revealed strong and progressive enrichment of the D2.OR/D2A1 dormancy signature over the 28-day course following Her2 downregulation in vitro (**Fig. 5A**, p=1.88e-09). This enrichment was reversible following doxycycline readdition, which reactivates Her2 signaling and induces dormant tumor cells to re-enter the cell cycle (**Fig. 5A**). The D2.OR-

bioRxiv preprint doi: https://doi.org/10.1101/2023.01.31.526529; this version posted February 3, 2023. The copyright holder for this preprint (which was not certified by peer review) is the author/funder, who has granted bioRxiv a license to display the preprint in perpetuity. It is made available under aCC-BY-NC-ND 4.0 International license.

329 derived dormancy signature was also enriched in a dormancy-specific manner in dormant
330 *MTB/TAN* and *MTB/TWNT* RTCs in vivo 28 days following oncogene downregulation vs. either
331 PTCs (*p*=7.4e-05, 1.7e-05, respectively) or recurrent tumor cells (*p*=6.2e-04, 1.1e-03,
332 respectively) (**Fig. S5A**).

333 Next, we asked what gene ontology terms were enriched within the D2.OR-derived
334 dormancy signature. As observed for the core RTC signature derived from therapy-associated
335 dormancy models, the D2.OR dormancy signature was enriched for multiple pathways relating
336 to ECM, proteoglycan, and GAG-related gene ontology terms (**Fig. 5B**, highlighted in red).
337 These data indicate that dormancy-associated gene expression signatures are strongly
338 enriched for ECM-related pathways in general, and proteoglycan and glycosaminoglycan-
339 related pathways in particular, irrespective of whether the dormant state was induced by the
340 microenvironment or associated with therapy.

341 D2.OR cells persist as dormant single cells over the course of 12 days when grown on
342 basement membrane extract (BME), whereas D2A1 cells generate proliferative, spindle-shaped
343 outgrowths under these same conditions[20]. Addition of Collagen I (Col I) to BME induces
344 dormant D2.OR cells to resume proliferation and generate D2A1-like spindle-shaped colonies[20].
345 Using this system, we asked whether the dormant behavior of D2.OR cells in 3D culture is
346 regulated by B3GALT6-mediated proteoglycan synthesis.

347 D2.OR and D2.A1 cells transduced with a sh*B3galt6* hairpin exhibited >80% knock-down
348 of *B3galt6* transcripts (**Fig. S5B**). D2.OR cells transduced with sh*B3galt6* or control
349 sh*Scrambled* hairpins were then overlaid on BME with or without addition of Col I. While the
350 numbers of viable sh*B3galt6* and sh*Scrambled* cells each decreased over the 12-day course,
351 *B3galt6* knockdown resulted in progressive and marked decreases in cell number at D8
352 (*p*=0.022) and D12 (*p*=0.0004) compared to control cells (**Fig. 5C, D**).

353 As anticipated, sh*Scrambled* D2.OR cells plated on BME + col I displayed increased
354 viable cell numbers over this same time course (**Fig. 5E, F**). *B3galt6* knockdown in D2.OR cells

bioRxiv preprint doi: https://doi.org/10.1101/2023.01.31.526529; this version posted February 3, 2023. The copyright holder for this preprint (which was not certified by peer review) is the author/funder, who has granted bioRxiv a license to display the preprint in perpetuity. It is made available under aCC-BY-NC-ND 4.0 International license.

yielded marked reductions in the numbers of viable tumor cells at D4, D8, and D12 compared to (p<0.0001) sh*Scrambled* controls. Indeed, the Col I-induced increase in number of D2.OR cells was entirely abrogated by *B3galt6* knockdown, as viable D2.OR sh*B3galt6* cells failed to increases in number when grown under these conditions (**Fig. 5E, F**). Additionally, while sh*Scrambled* D2.OR cells formed spindle-like colonies when grown on BME + Col I, sh*B3galt6* cells failed to do so. These data suggest that B3GALT6 is required for both the viability of dormant tumor cells and their outgrowth.

We next performed analogous 3D assays using D2A1 cells. When grown on BME, a significant decrease in viable cell number was observed for sh*B3galt6* vs. sh*Scrambled* D2A1 cells at D12 (p=0.003), and sh*B3galt6* D2A1 cells failed to exhibit the characteristic spindle-like morphology adopted by sh*Scrambled* D2A1 cells that is associated with colony outgrowth (**Fig. S5C, D**). Notably, this same difference in phenotype was observed in sh*B3galt6* D2A1 cells (**Fig. S5E**) grown on BME + Col I. Moreover, a progressive decrease in viable cell numbers was observed for sh*B3galt6* D2A1 cells grown on BME + Col I at D4 (p=0.0014), D8 (p=0.0002), and D12 (p<0.0001) compared to control cells (**Fig. S5F**). These data indicate that, B3GALT6 is required for cell viability, as well as outgrowth, in proliferative D2A1 cells. Taken together, these findings suggest that B3GALT6 is a critical regulator of cell survival in dormant tumor cells, irrespective of whether dormancy is therapy-associated or induced by the microenvironment.

Heparan sulfate synthesis is upregulated during dormancy and associated with poor outcomes in breast cancer patients

In light of our observations implicating B3GALT6-mediated proteoglycan biosynthesis as a key determinant of dormant tumor cell persistence in therapy-associated and microenvironment-induced models of dormancy, we next asked how proteoglycan synthesis is regulated during dormancy.

bioRxiv preprint doi: https://doi.org/10.1101/2023.01.31.526529; this version posted February 3, 2023. The copyright holder for this preprint (which was not certified by peer review) is the author/funder, who has granted bioRxiv a license to display the preprint in perpetuity. It is made available under aCC-BY-NC-ND 4.0 International license.

Because B3GALT6 catalyzes the synthesis of a linker that is common to, and required for, the production of both heparan sulfate and chondroitin sulfate (**Fig. 3A**), we assessed the biosynthesis of these GAGs under dormancy conditions. First, we applied heparan sulfate and chondroitin/dermatan sulfate KEGG mRNA biosynthesis signatures to IVD gene expression data derived from Her2-dependent cells. This revealed that enzymes involved in heparan sulfate synthesis and modification are upregulated (**Fig. S6A**) – whereas those involved in chondroitin/dermatan sulfate synthesis and modification are downregulated (**Fig. S6B**) – during dormancy in vitro.

Addition of the hexosamine residue *N*-Acetylglucosamine (GlcNAc) to the proteoglycan tetrasaccharide linker results in heparan sulfate synthesis, whereas addition of *N*-Acetylgalactosamine (GalNAc) to this linker results in chondroitin/dermatan sulfate synthesis[49]. Notably, the enzymes (*Extl2*, *Extl3*) that direct heparan sulfate synthesis by catalyzing the addition of GlcNAc to the tetrasaccharide linker are reversibly upregulated during dormancy in vitro (**Fig. S6C**); in contrast, the enzymes (*Csgalnact1*, *Csgalnact2*) that direct chondroitin sulfate synthesis by catalyzing the addition of GalNAc to this linker are reversibly downregulated during dormancy (**Fig. S6D**). Consistent with this, we identified the heparan sulfate polymerase *Ext2* as a hit in the CRISPR-Cas9 screen, whereby sgRNAs targeting *Ext2* were selected against during dormancy, as were sgRNAs targeting *B3galt6* (**Fig. 2D**). In contrast, negative selection for the chondroitin sulfate polymerase *Chpf* was not observed in our screen (**Fig. S2C**). These associations suggest the preferential synthesis of heparan sulfate rather than chondroitin/dermatan sulfate in dormant RTCs.

To quantify levels of heparan sulfate and chondroitin sulfate GAGs as a function of dormancy, we performed liquid chromatography-mass spectrometry (LC/MS) on cell lysates isolated at baseline (D0, proliferative) or post-doxycycline withdrawal (D7, dormant). Heparan sulfate was readily detectable in Her2-dependent tumor cells at D0 and its levels were significantly higher in dormant tumor cells at D7 (p<0.0001) (**Fig. 6A**). In contrast, chondroitin

bioRxiv preprint doi: https://doi.org/10.1101/2023.01.31.526529; this version posted February 3, 2023. The copyright holder for this preprint (which was not certified by peer review) is the author/funder, who has granted bioRxiv a license to display the preprint in perpetuity. It is made available under aCC-BY-NC-ND 4.0 International license.

406 sulfate levels were >100-times lower than heparan sulfate at baseline (D0) and did not change
407 significantly during dormancy (**Fig. 6A**).

408 We next evaluated GAG levels in vivo as a function of dormancy using heparan or
409 chondroitin sulfate-specific antibodies. We first confirmed the specificity of these antibodies by
410 demonstrating that pre-treatment of tissue sections with heparin lyase or chondroitinase
411 eliminated the signal detected for heparan sulfate or chondroitin sulfate, respectively (**Fig. S6E,**
412 **F**). Immunofluorescence staining revealed that Her2-dependent PTCs (green) expressed
413 heparan sulfate but not chondroitin sulfate (**Fig. 6B, C**; **S6E, F**). Moreover, heparan sulfate
414 levels increased in dormant tumor cells at D7, whereas chondroitin sulfate remained
415 undetectable (**Fig. 6B**, **C**). Thus, both LC/MS and immunofluorescence data demonstrate an
416 increase in heparan sulfate abundance during dormancy, both in vitro and in vivo.

417 Defects in differentiation resulting from heparan sulfate impairment in myoblasts[50] and
418 mouse embryonic stem cells[51] in vitro have been reported to be partially rescued by the addition
419 of exogenous heparin, a highly sulfated heparan sulfate variant. Therefore, we performed an
420 analogous experiment to determine whether heparin addition could rescue the impaired cell
421 survival observed in B3GALT6-depleted cells, as would be predicted if heparan sulfate
422 promotes the survival of dormant tumor cells.

423 We harvested Her2-dependent sg*Rosa* and sg*B3galt6* cells at baseline (D0,
424 proliferative) and in cells treated with vehicle, low-dose heparin, or high-dose heparin for 7 days
425 post-doxycycline withdrawal (D7, dormant). As above, sg*B3galt6* cells exhibited decreased
426 survival at D7 compared to control cells **(Fig. 6D)**. Consistent with reports that heparin
427 supplementation in heparan sulfate-replete cells may dampen signaling by competing with
428 endogenous heparan sulfate[52], we observed that both low- and high-dose heparin treatment in
429 sg*Rosa* cells modestly decreased viable RTC number vs. vehicle-treated controls (**Fig. 6D**). In
430 contrast, exogenous addition of high-dose heparin to sg*B3galt6* RTCs markedly increased the
431 number of viable tumor cells at D7 vs. vehicle-treated controls (p<0.0001) (**Fig. 6D**). These data

bioRxiv preprint doi: https://doi.org/10.1101/2023.01.31.526529; this version posted February 3, 2023. The copyright holder for this preprint (which was not certified by peer review) is the author/funder, who has granted bioRxiv a license to display the preprint in perpetuity. It is made available under aCC-BY-NC-ND 4.0 International license.

indicate that heparin supplementation is sufficient to rescue the survival defect induced by loss of B3GALT6 in dormant RTCs.

To extend these findings to a microenvironment-induced model of dormancy, we plated D2.OR cells transduced with sh*B3galt6* or control sh*Scrambled* hairpins in 3D in the presence of vehicle or heparin. As before, loss of B3GALT6 resulted in a pronounced survival defect in dormant D2.OR cells grown on BME (**Fig. 6D**). Notably, addition of exogenous heparin partially rescued the decrease in viable cell number observed in dormant D2.OR sh*B3galt6* cells vs. sh*Scrambled* at D5 (p=0.003) and D10 (p=0.0009) (**Fig. 6E, F**). Additionally, when D2.OR cells were plated under outgrowth conditions (BME + Col I), heparin potently rescued the decrease in cell numbers observed in dormant D2.OR sh*B3galt6* cells vs. sh*Scrambled* at D5 (p<0.0001) and D10 (p<0.0001) (**Fig. 6G**). These findings are concordant with those observed in Her2-dependent cells and consistent with the hypothesis that heparan sulfate GAGs are required for maintaining dormant RTC survival and subsequent outgrowth. However, heparin failed to rescue the rounded morphology associated with sh*B3galt6*, suggesting that D2.OR cells may transduce the Collagen I signal to stimulate the spindle-like morphology of outgrowths independently of heparin/heparan sulfate. (**Fig. 6H**).

To this point, our functional data in preclinical models suggested a role for heparan sulfate, but not chondroitin sulfate, in dormant tumor cell survival and we had observed the concordant dormancy-associated upregulation of a heparan sulfate KEGG mRNA biosynthesis signature, expression of rate-limiting enzymes for heparan sulfate synthesis, and levels of heparan sulfate, as well as a lack of dormancy-associated changes in these same features for chondroitin sulfate. Therefore, we applied the KEGG heparan sulfate and chondroitin/dermatan sulfate mRNA biosynthetic signatures to gene expression data from primary breast cancers in ~4400 patients with known recurrence outcomes[38]. Strikingly, and consistent with a role for heparan sulfate in enhancing tumor cell fitness during dormancy and recurrence, the expression of heparan sulfate biosynthetic enzymes in early stage primary breast cancers was strongly

bioRxiv preprint doi: https://doi.org/10.1101/2023.01.31.526529; this version posted February 3, 2023. The copyright holder for this preprint (which was not certified by peer review) is the author/funder, who has granted bioRxiv a license to display the preprint in perpetuity. It is made available under aCC-BY-NC-ND 4.0 International license.

associated with poorer recurrence-free survival (overall *p* value=2.2e-04) (**Fig. 6I**). In contrast, no association was observed between recurrence-free survival and expression chondroitin/dermatan sulfate biosynthetic enzymes (**Fig. 6J**). These data provide further evidence specifically implicating heparan sulfate, rather than chondroitin sulfate, biosynthesis in promoting breast cancer recurrence in patients.

Our findings demonstrate that enzymes involved in heparan sulfate synthesis, as well as total heparan sulfate levels, are upregulated in dormant tumor cells both in vivo and in vitro and that heparin supplementation partially rescues the survival defect induced by B3GALT6 loss in RTCs both in the context of therapy-associated dormancy and microenvironment-induced dormancy. In contrast, we found that chondroitin sulfate levels are orders of magnitude lower than heparan sulfate in tumor cells and are not upregulated during dormancy. Consistent with this, the enzymes involved in chondroitin sulfate synthesis are downregulated during dormancy. Taken together with our other findings, these data suggest a selective and essential role for heparan sulfate in mediating dormant RTC survival.

Heparan sulfate 6-*O*-sulfation is selectively upregulated during dormancy and potentiates FGF1 signaling

Having identified a key role for B3GALT6-mediated heparan sulfate biosynthesis in promoting RTC survival, we asked if heparan sulfate undergoes dynamic modifications during dormancy, as was suggested by the reversible upregulation of gene expression for modifying enzymes, such as sulfotransferases (*e.g.*, *Ndst2*, *Hs2st1*, *Hs6st1*), within the heparan sulfate signature (**Fig. S6C**). Accordingly, we examined the extent and sites of heparan sulfation since this modification is a key determinant of the ligand binding properties of GAG side chains[23,53].

To accomplish this, we isolated cell lysates from Her2-dependent cells grown in vitro at D0 (*baseline*), D7 and D28 (*deinduction*), and D28+ (*reinduction*) and performed glycan reductive isotope labeling followed by LC/MS (GRIL-LC/MS)[54] (**Fig. S7A**). This revealed a

bioRxiv preprint doi: https://doi.org/10.1101/2023.01.31.526529; this version posted February 3, 2023. The copyright holder for this preprint (which was not certified by peer review) is the author/funder, who has granted bioRxiv a license to display the preprint in perpetuity. It is made available under aCC-BY-NC-ND 4.0 International license.

significant and progressive increase in the average sulfation level per heparan sulfate-derived disaccharide at D7 and D28 of dormancy vs. D0 baseline (p<0.0001), which remained elevated after 72 hr of Her2 reinduction (**Fig. S7B**). This dormancy-associated increase in sulfation indicates that, in addition to increased overall levels of heparan sulfate GAGs during dormancy, the extent to which these GAGs are sulfated is also dynamically upregulated in RTCs.

Next, we wished to determine whether dormancy-selective patterns of heparan sulfation were present. Of the 3 (out of 4 total) sulfation sites on heparan sulfate-derived disaccharides that we interrogated (**Fig. 7A-C; S7C**), 6-*O*-sulfation exhibited the most dramatic fold-increase in abundance during dormancy **(Fig. 7A-D)**. We also examined the relative abundance of specific disaccharide motifs[55] as a function of dormancy (**Fig. S7D, E**). Only D2S6 and D0A6 disaccharides showed upregulation during dormancy in a manner that was reversible following exit of cells from the dormant state (**Fig. S7F, G**). This indicates that 6-*O*-sulfation on glucosamine tends to co-occur in non-sulfated uronic acid-*N*-acetylated glucosamine (D0A6) or 2-*O*-sulfated uronic acid-*N*-sulfated glucosamine (D2S6) disaccharides.

Heparan 6-*O*-sulfation has been reported to promote FGF signaling by increasing the binding affinity of some FGF ligands for heparan sulfate in the ternary heparan sulfate-FGF-FGFR complex that is required for FGF signaling[56,57] (**Fig. S7H**). To identify which FGF ligands are expressed in dormant tumor cells in an abundant, but reversible, manner we interrogated the expression of the 15 paracrine FGFs that require heparin/heparan sulfate as a co-factor for signaling[58]. This revealed that FGF1 is dramatically and persistently upregulated (>10-fold) during dormancy as early as 3 days following doxycycline withdrawal, and that its expression is potently suppressed within 48 hr of doxycycline re-addition (D7+, D14+, D28+) (**Fig. 7E**). Other notable FGF ligands included FGF2, which displayed only minor upregulation during dormancy that was not reversible, and FGF7, which displayed reversibility but was expressed at low levels with only modest dormancy-associated upregulation (**Fig. S7I**).

bioRxiv preprint doi: https://doi.org/10.1101/2023.01.31.526529; this version posted February 3, 2023. The copyright holder for this preprint (which was not certified by peer review) is the author/funder, who has granted bioRxiv a license to display the preprint in perpetuity. It is made available under aCC-BY-NC-ND 4.0 International license.

Our finding that FGF1 expression is markedly upregulated in dormant tumor cells was particularly striking in light of recent data identifying heparan 6-*O*-sulfation as a strong binding site for FGF1, but not FGF2[59]. This suggested the possibility that dormant tumor cells might be specifically dependent on heparan sulfate 6-*O*-sulfation as a consequence of its interaction with FGF1.

To test whether FGF1 regulates RTC survival, we determined the number of dormant RTCs that survived Her2 downregulation in vitro following the depletion of endogenous FGF1 using CRISPR-Cas9-based deletion. After confirming successful editing by *Fgf1* sgRNAs by ICE analysis (**Fig. S7J**), we performed an IVD assay using Her2-dependent-Cas9 cells transduced with sg*Fgf1* or sg*Rosa*. Deletion of FGF1 further accentuated the decrease in viable RTC numbers that occurs at D7 (*deinduction*) vs. D0 (*baseline*) when compared to the sg*Rosa* controls (**Fig. S7K**). This suggests that tumor cell-autonomous FGF1 signaling promotes dormant RTC survival.

To determine whether FGF acts via heparan 6-*O*-sulfation to mediate B3GALT6-associated RTC survival, we examined the expression of the three sulfotransferases, *Hs6st1-3,* that catalyze 6-*O*-sulfation (**Fig. S7H**), particularly those on the D2S6 and D0A6 6-*O*-sulfated disaccharide motifs[53,56] identified above. Of these, only *Hs6st1* was found to be abundantly expressed in Her2-dependent cells and only *Hs6st1* was reversibly upregulated during dormancy (**Fig. S7L**). Notably, *Hs6st1* was identified as a putative pro-survival hit in our CRISPR-Cas9 screen, which exhibited increasingly apparent effects at later dormancy time points (**Fig. 2D, 7F**).

We also evaluated the expression of the four FGFRs, *Fgfr1-4*, that participate in FGF signaling. Of these, *Fgfr1* and *Fgfr2* are abundantly expressed in Her2-dependent cells and are each reversibly upregulated during dormancy (**Fig. S7L**); *Fgfr2* was upregulated ~4-fold during dormancy, whereas *Fgfr1* was upregulated ~1.5-fold. Although FGF1 can signal through both FGFR1 and FGFR2, *Fgfr2* was identified as a putative pro-survival hit in our CRISPR-Cas9

bioRxiv preprint doi: https://doi.org/10.1101/2023.01.31.526529; this version posted February 3, 2023. The copyright holder for this preprint (which was not certified by peer review) is the author/funder, who has granted bioRxiv a license to display the preprint in perpetuity. It is made available under aCC-BY-NC-ND 4.0 International license.

screen, whereas sgRNAs targeting *Fgfr1* displayed no selection (**Fig. 2D, S2C, 7F**). Accordingly, we hypothesized that 6-*O*-sulfated heparan sulfate and FGFR2 may act together to promote FGF1 signaling and RTC survival, and prioritized studies of FGFR2 as a candidate for maintaining dormant RTC survival.

To determine whether heparan 6-*O*-sulfation and FGFR2 act in concert to promote FGF1 signaling and dormant RTC survival, we first sought to evaluate FGF activity in dormant tumor cells in vitro, as well as the effect of inhibiting heparan sulfate biosynthesis or 6-*O*-sulfation on FGF signaling.

After confirming successful editing by *Hs6st1* and *Fgfr2* sgRNAs by ICE analysis (**Fig. S7M**), we performed an IVD assay using Her2-dependent-Cas9 cells transduced with sg*B3galt6*, sg*Hs6st1*, sg*Fgfr2*, or sg*Rosa*. We reasoned that if increased heparan sulfate synthesis and 6-*O*-sulfation by dormant RTCs enhances endogenous FGF signaling, then impairing heparan sulfate synthesis (sg*B3galt6*), or 6-*O*-sulfation (sg*Hs6st1*), should attenuate FGF signaling (**Fig. S7N**). Furthermore, we predicted that if enhanced FGF signaling in dormant cells is mediated by FGFR2, depleting *Fgfr2* should also attenuate FGF signaling during dormancy.

To test this hypothesis, we assessed levels of activated ERK1/2[60] in each of the above genetic contexts, using two sgRNAs each for sg*B3galt6*, sg*Hs6st1*, and sg*Fgfr2*. As anticipated, pERK1/2 levels normalized to total ERK1/2 were >10-fold higher in Her2-dependent proliferating cells at D0 (*baseline*) compared to D4 or D7 dormancy time points (**Fig. 7G, S7O**). Moreover, pERK1/2:ERK1/2 levels in the presence of Her2 expression (D0) were largely unaffected by deletion of *B3galt6*, *Hs6st1*, or *Fgfr2*. In contrast, pERK1/2:ERK1/2 levels were significantly and progressively diminished in sg*B3galt6*, sg*Hs6st1*, and sg*Fgfr2* cells compared to *sgRosa* controls following Her2 downregulation (*deinduction*) induced by doxycycline withdrawal (**Fig. 7G, S7O**). This additional impairment of pERK1/2:ERK1/2 levels caused by deletion of components of the FGF signaling pathway that are expressed in RTCs in a dormancy-specific

bioRxiv preprint doi: https://doi.org/10.1101/2023.01.31.526529; this version posted February 3, 2023. The copyright holder for this preprint (which was not certified by peer review) is the author/funder, who has granted bioRxiv a license to display the preprint in perpetuity. It is made available under aCC-BY-NC-ND 4.0 International license.

manner is consistent with a model in which endogenous FGF signaling is active during dormancy, and requires B3GALT6, HS6ST1, and FGFR2 for its maintenance.

Upregulation of heparan sulfate 6-*O*-sulfation during dormancy promotes RTC survival and recurrence by potentiating FGF signaling

Given the above findings, we assessed whether the addition of exogenous FGF ligands can increase the number of viable RTCs in vitro. Indeed, we found that addition of FGF1 to sg*Rosa* cells for 4 days initiated concurrently with doxycycline withdrawal resulted in a near doubling of the number of viable RTCs compared to vehicle controls (dotted line) (**Fig. S7P**). This FGF1-induced increase in viable dormant RTCs was impaired in sg*B3galt6*, sg*Hs6st1*, and sg*Fgfr2* cells vs. sg*Rosa* controls (**Fig. S7P**). These findings suggest that heparan sulfate (synthesized by B3GALT6), particularly 6-*O*-sulfation (catalyzed by HS6ST1), as well as FGFR2 are key components of FGF signal transduction in dormant RTCs.

Next, we asked if the impaired response to FGF1 in sg*B3galt6* and sg*Hs6st1* RTCs compared to sg*Rosa* RTCs could be rescued by the addition of heparin, which is natively sulfated, including at the 6-*O* site. We treated Her2-dependent tumor cells with FGF1, heparin, or a combination of FGF1 + heparin for 7 days post-doxycycline withdrawal (D7, dormant). We found that heparin could rescue the blunted response to exogenous FGF1 stimulation observed in sg*B3galt6* and sg*Hs6st1* cells (**Fig. 7H**). These data are consistent with a model wherein heparan 6-*O*-sulfation potentiates FGF signaling to promote the survival of dormant RTCs in vitro.

We wished to determine whether heparan 6-*O*-sulfation and FGF signaling promote dormant RTC viability and tumor recurrence as suggested by the CRISPR screen results (**Fig. 2D, 7F**). We assessed viable RTC number for sg*Rosa*, sg*B3galt6*, sg*Hs6st1*, and sg*Fgfr2*-transduced Her2-dependent-Cas9 cells at D7 (*deinduction*). Consistent with our hypothesis, dormant tumor cells deleted for each of these genes exhibited significantly impaired survival

bioRxiv preprint doi: https://doi.org/10.1101/2023.01.31.526529; this version posted February 3, 2023. The copyright holder for this preprint (which was not certified by peer review) is the author/funder, who has granted bioRxiv a license to display the preprint in perpetuity. It is made available under aCC-BY-NC-ND 4.0 International license.

587 during dormancy vs. sg*Rosa* control cells (**Fig. S7Q**). This suggests that heparan 6-*O*-sulfation
588 potentiates endogenous FGF signaling mediated by FGFR2 to promote the survival of dormant
589 RTCs in vitro.

590 To extend these findings in vivo, we injected GFP-labeled sg*Rosa*, sg*Hs6st1*, and
591 sg*Fgfr2* Her2-dependent-Cas9 cells into mice maintained on doxycycline. Her2-driven PT
592 samples (*baseline*) as well as D7 RL samples following doxycycline withdrawal were harvested
593 for TUNEL staining. This revealed a significant increase in the percentage of TUNEL+ sg*Hs6st1*
594 (p=0.003) and sg*Fgfr2* (p=0.04) tumor cells in D7 RL vs. sg*Rosa* controls (**Fig. 7I, J**). In
595 contrast, we found no significant differences in the percentage of TUNEL+ tumor cells in
596 sg*Hs6st1,* sg*Fgfr2,* and *sgRosa* PT samples. These data indicate that sg*Hs6st1* and sg*Fgfr2*
597 dormant RTCs display a selective impairment in RTC, but not PTC, survival compared to the
598 controls, in a manner analogous to our findings for sg*B3galt6*.

599 Finally, to determine the impact of HS6ST1 and FGFR2-mediated pro-survival effects on
600 tumor recurrence, we performed recurrence-free survival assays in mice bearing dormant RLs
601 derived from sg*Hs6st1* or sg*Fgfr2* Her2-dependent tumor cells. Analogous to our findings for
602 sg*B3galt6*, mice bearing dormant RLs containing sg*Hs6st1* or *Fgfr2* tumor cells exhibited
603 delayed recurrence-free survival compared to sg*Rosa* controls (p=0.02, HR=0.42; and p=0.006,
604 HR=0.35, respectively) (**Fig. 7K**). This demonstrates that HS6ST1 and FGFR2 are each
605 required for efficient tumor recurrence.

606 In aggregate, the above studies are consistent with a model in which HS6ST1 is
607 reversibly upregulated during dormancy, which results in the selective upregulation of heparan
608 sulfate 6-*O*-sulfation in dormant RTCs and potentiation of FGF1 signaling via FGFR2, thereby
609 enhancing dormant RTC survival. This, in turn, promotes tumor recurrence, as reflected by the
610 delay in the median time-to-recurrence observed for tumor cells deleted for either *Hs6st1* or
611 *Fgfr2.*
612

bioRxiv preprint doi: https://doi.org/10.1101/2023.01.31.526529; this version posted February 3, 2023. The copyright holder for this preprint (which was not certified by peer review) is the author/funder, who has granted bioRxiv a license to display the preprint in perpetuity. It is made available under aCC-BY-NC-ND 4.0 International license.

Discussion

Residual tumor cells (RTCs) that persist following primary tumor therapy have long been recognized as the precursors of treatment-refractory recurrent disease that determines patient mortality. While a small number of post-adjuvant clinical trials to identify and target dormant RTCs in early stage breast cancer patients are currently underway[61,62], there is a pressing need to identify unique biological vulnerabilities of dormant RTCs.

In this study, we address this unmet clinical need by identifying novel, actionable dependencies of RTC fitness that could be leveraged to prevent tumor recurrence. Utilizing a combination of in vivo and in vitro derived gene expression data from mouse models and breast cancer patients, a CRISPR-Cas9-based screen, and functional validation studies in mouse models for tumor dormancy and recurrence, we found that dormant RTCs create – in a cell autonomous manner – an extracellular environment that is conducive to their own survival. In particular, we determined that dormant RTCs selectively upregulate the B3GALT6-mediated synthesis of heparan sulfate proteoglycans in both therapy-associated and microenvironment-induced models of dormancy. Underscoring the clinical relevance of these data, we observed that increased heparan sulfate synthesis in primary tumors in patients is associated with poor recurrence-free survival. Mechanistically, we found that dormant RTCs reversibly upregulate not only B3GALT6-mediated heparan sulfate synthesis, but also HS6ST1-mediated 6-*O*-sulfation of heparan sulfate proteoglycans, as well as *Fgf1* and *Fgfr2* expression, in a dormancy-specific manner. These orchestrated effects result in enhanced FGF1 signaling via FGFR2, enhanced dormant RTC survival, and accelerated tumor recurrence. In aggregate, our findings identify the B3GALT6-heparan sulfate/HS6ST1-6-*O*-sulfation/FGF1-FGFR2 signaling axis (**Fig. S7N**) as a potential therapeutic target for preventing tumor recurrence from dormant RTCs.

Proteoglycans have pleiotropic functions in both normal physiology and during cancer initiation and progression[23]. Individual proteoglycans have been implicated as regulators of tumor cell growth, angiogenesis, epithelial-to-mesenchymal transition, anoikis, extravasation,

bioRxiv preprint doi: https://doi.org/10.1101/2023.01.31.526529; this version posted February 3, 2023. The copyright holder for this preprint (which was not certified by peer review) is the author/funder, who has granted bioRxiv a license to display the preprint in perpetuity. It is made available under aCC-BY-NC-ND 4.0 International license.

and colonization of metastatic locations[63]. In contrast, little is known about potential roles for proteoglycans during the dormant phase of cancer progression[64], and fewer studies still have dissected the function of the protein core of proteoglycans from that of their GAG chains.

Our findings identify B3GALT6 as a potent regulator of dormant RTC survival and recurrence. To date, a role for B3GALT6 in cancer has not been reported. Because B3GALT6 is essential for synthesis of the tetrasaccharide required for covalent linkage of GAG chains to their protein core[28], genetic deletion of *B3galt6* permits the role of GAGs in tumor progression to be specifically investigated, as opposed to their protein cores. Prior studies of B3GALT6 in vertebrate models have been limited to genetic loss in a zebrafish model[46] generated for study of two pathogenic conditions observed in patients with biallelic loss of *B3GALT6*: spEDS and SEMD-JL1[29,31]. Accordingly, while zebrafish with *b3galt6* loss-of-function recapitulate the connective tissue defects observed in spEDS and SEMD-JL1 patients, the extent to which the pathways underlying B3GALT6-mediated functions in connective tissues, and those explaining the dependence of dormant epithelial tumor cells on this enzyme, are shared – if at all – remains to be determined.

The levels and spatial patterns of heparan sulfation strongly influence the extracellular ligand milieu and the extent to which proteoglycans elicit signaling in cells[26]. In addition to the dormancy-associated upregulation of heparan sulfate proteoglycans in our model, we discovered an upregulation of the extent of heparan sulfation in dormant residual tumor cells. A recent study in melanoma cells identified increased levels of a transporter of the sulfate donor PAPS (*i.e.*, SLC35B2) and downstream heparan sulfation as a dependency of melanoma cells that are refractory to MAPK pathway inhibition[65]. In light of our study, these data may suggest the possibility that increased heparan sulfation may constitute an adaptive mechanism of drug resistance in multiple cancer types, although the site of heparan sulfation and dependence of this phenotype on FGF signaling were not addressed in this study.

bioRxiv preprint doi: https://doi.org/10.1101/2023.01.31.526529; this version posted February 3, 2023. The copyright holder for this preprint (which was not certified by peer review) is the author/funder, who has granted bioRxiv a license to display the preprint in perpetuity. It is made available under aCC-BY-NC-ND 4.0 International license.

Heparan 6-*O* sulfation is required for formation of the ternary heparan sulfate-FGF-FGFR complex and, therefore, FGF pathway activity[56,57]. In particular, 6-*O*-sulfation is a strong determinant of FGF1 binding[59]. FGF signaling is classically thought to play a mitogenic function in tumor cells[8,66]. However, recent data suggest a context-dependent role for FGF signaling in promoting breast cancer therapy resistance and growth arrest. FGF2 derived from osteogenic cells in the bone marrow can suppress the expression of estrogen receptor (ER) in disseminated breast cancer cells via FGFR1, rendering them resistant to endocrine therapy[67]. Furthermore, exogenously-derived FGF2 induces cell cycle arrest in ER+ breast cancer cell lines, such as MCF7 and T47D[68], and can induce the expression of the pro-dormancy transcription factor ZFP281 in early disseminated cancer cells[69]. In contrast to these examples in which FGF2 can promote dormancy predominantly via FGFR1, our data suggest dormant RTC survival is mediated by tumor cell-autonomous FGF1 in a heparan sulfate-FGFR2 dependent manner. In this regard, we found that genetic depletion of FGFR2 induced RTC apoptosis and significantly delayed recurrence. Consistent with this, our CRISPR screen identified *Fgfr2*, but not *Fgfr1*, as a vulnerability in dormant RTCs. These data suggest the intriguing possibility that highly selective FGFR2 pharmacological inhibitors currently in clinical trials in other solid tumors (NCT04526106[70], NCT04071184[71]) could be leveraged in the adjuvant or post-adjuvant setting, to exploit the dependency of dormant RTCs on FGF signaling for their survival and recurrence.

Although heparan 6-*O*-sulfation has been reported to increase the affinity of VEGFA binding to VEGFR2[72], both VEGFA and VEGFR2 gene expression levels are downregulated during dormancy in our model, thereby providing further evidence for the selective effects of FGF signaling in the context of dormancy and heparan 6-*O*-sulfation. Consistent with this, we have not observed evidence supporting angiogenic impairment as a mechanism of dormancy in our model[6]. Notably, desulfation of heparan sulfate at the 6-*O* position is catalyzed by the sulfatases, SULF1 and SULF2[53]. As such, our data demonstrating that heparan 6-*O*-sulfation is

bioRxiv preprint doi: https://doi.org/10.1101/2023.01.31.526529; this version posted February 3, 2023. The copyright holder for this preprint (which was not certified by peer review) is the author/funder, who has granted bioRxiv a license to display the preprint in perpetuity. It is made available under aCC-BY-NC-ND 4.0 International license.

690 preferentially increased during dormancy is compatible not only with models in which
691 sulfotransferase activity is upregulated, as we have shown occurs during dormancy, but also
692 with models in which sulfatase activity is downregulated. Although we observe no
693 downregulation of *Sulf1* and *Sulf2* levels in dormancy, further investigation into the regulation of
694 6-*O*-sulfation during breast cancer progression is a promising avenue of future research.

695 Intriguingly, our studies implicate heparan sulfate, rather than chondroitin sulfate, as the
696 key GAG responsible for promoting RTC fitness. Although our study is focused on the glycan
697 component of proteoglycans, the core protein may also play an important role beyond serving
698 as a scaffold for the attachment of GAGs. Indeed, sequences within the core protein can
699 influence the stoichiometry[73] and sulfation pattern of GAG chains[72], with important biological
700 consequences[74]. The heparan sulfate proteoglycan family orchestrates diverse physiological
701 functions[26] and includes transmembrane syndecans (SDC1-4), 6 glycophosphatidylinositol
702 (GPI)-anchored glypicans (GPC1-6), as well as secreted perlecan, agrin, and collagen XVIII that
703 are deposited in the extracellular matrix[25]. Additionally, betaglycan (also known as TGFBR3)
704 and a splice variant of CD44 (CD44v3) can be modified by GAGs, including heparan sulfate,
705 and act as 'part-time' proteoglycans[25]. Determining which heparan sulfate proteoglycans
706 contribute to RTC survival in breast cancer models, and whether their functions are dependent
707 on the heparan sulfate GAG are intriguing directions to pursue.

708 In conclusion, our study identifies a dormancy-specific function for the B3GALT6-
709 heparan sulfate/HS6ST1-6-*O*-sulfation/FGF1-FGFR2 signaling axis in maintaining RTC survival.
710 In addition to ascribing a critical role to an understudied class of compounds, namely
711 glycosaminoglycans, in breast cancer progression, our study leverages this information to
712 identify novel therapeutic vulnerabilities for depleting RTCs in an effort to mitigate the
713 development of incurable recurrences.
714
715

bioRxiv preprint doi: https://doi.org/10.1101/2023.01.31.526529; this version posted February 3, 2023. The copyright holder for this preprint (which was not certified by peer review) is the author/funder, who has granted bioRxiv a license to display the preprint in perpetuity. It is made available under aCC-BY-NC-ND 4.0 International license.

Acknowledgments

We thank Dr. Junwei Shi and his laboratory for their advice on developing and performing the CRISPR-Cas9 screen, Dr. Mikala Egeblad for the gift of D2.OR and D2A1 cells, Jianping Wang for histology assistance, Mousumi Paulchakrabarti for GRIL-LC/MS assistance, and Cuyler Luck as well as members of the Chodosh laboratory for their invaluable input that led to the development of techniques used in this study. This project was supported in part by grants from the NIH and the Breast Cancer Research Foundation to L.A.C. and by a grant from DOD to A.S.

Author contributions

Conceptualization, A.S., J.D.E., and L.A.C.; Methodology, A.S., M.L., B.C., T.P., D.K.P., C.J.S., G.K.B., T.T., B.B., M.E., and F.E.M.; Investigation, A.S., M.L., B.C., T.P., and D.K.P.; Writing, A.S. and L.A.C.; Funding Acquisition, A.S. and L.A.C.

Declaration of interests

L.A.C. has served as an expert witness and consultant in litigation involving Teva Pharmaceuticals, Sanofi, Lilly, Whittaker, Clark and Daniels, Imerys, Colgate, and Sterigenics.

bioRxiv preprint doi: https://doi.org/10.1101/2023.01.31.526529; this version posted February 3, 2023. The copyright holder for this preprint (which was not certified by peer review) is the author/funder, who has granted bioRxiv a license to display the preprint in perpetuity. It is made available under aCC-BY-NC-ND 4.0 International license.

STAR Methods

In vitro assays

MTB/TAN-derived primary tumor cells were cultured in DMEM (Corning, Cat. # 10-017-CV) containing 10% super calf serum (GeminiBio, Cat. # 100-510), 1% Penicillin/Streptomycin (Thermo Fisher Scientific, Cat. # 15-140-122), 1% Glutamine (Thermo Fisher Scientific, Cat. # 25030081), 2mg/ml Doxycycline (RPI, Cat. # D43020-250.0), 5mg/ml Prolactin (NHPP, Cat. # NIDDK-oPRL-21), 5mg/ml Insulin (GeminiBio, Cat. # 700-112P), 10ug/ml EGF (Millipore, Cat. # E4127), 1mg/ml Hydrocortisone (Sigma, Cat. # H0396), 1mM Progesterone (Sigma, Cat. # P7556).

For in vitro dormancy experiments, cells were plated on D-3 in medium as above, transitioned to medium as above containing 1% super calf serum on D-2, and transitioned to medium containing 1% super calf serum and no Doxycycline on D0. Plates were harvested at dormancy deinduction time points as desired, while medium containing 1% super calf serum and no Doxycycline was replaced on remaining plates weekly. Reinduction plates were harvested at time points as desired following 48h or 72h treatment with medium containing 1% super calf serum and doxycycline as indicated in the figures.

D2.OR and D2A1 cells were a gift from Dr. Mikala Egeblad at Cold Spring Harbor Laboratories. These cells were maintained in in DMEM (Corning, Cat. # 10-017-CV) containing 10% fetal bovine serum (GeminiBio, Cat. # 100-106), 1% Penicillin/Streptomycin (Thermo Fisher Scientific, Cat. # 15-140-122).

Cell viability assays (2D and 3D) were performed as per manufacturer's instructions using the Cell Titer 96 Non-Radioactive Cell Proliferation Assay (Promega, Cat. # G4000) in 96-well plates.

3D assays

bioRxiv preprint doi: https://doi.org/10.1101/2023.01.31.526529; this version posted February 3, 2023. The copyright holder for this preprint (which was not certified by peer review) is the author/funder, who has granted bioRxiv a license to display the preprint in perpetuity. It is made available under aCC-BY-NC-ND 4.0 International license.

D2.OR and D2A1 cells were plated on top of a matrix of basement membrane extract (Cultrex 3D Basement Membrane Extract, Reduced Growth Factor, Trevigen Cat. # 3445-005-01) or a 1:1 ratio of basement membrane extract and neutralized type I collagen (Cultrex 3D Culture Matrix Rat Collagen I, Trevigen Cat. # 3447-020-01). For experiments in 96-well plates (Corning, Cat. # 353219), 50µl of the matrix was added per well and were solidified for 1h at 37°C. D2.OR and D2A1 cells were resuspended at 20,000 cells/ml in DMEM low glucose, low pyruvate medium (Thermo Fisher Scientific, Cat. # 11885092) containing 2% fetal bovine serum (GeminiBio, Cat. # 100-106), 2% basement membrane extract, 1% Penicillin/Streptomycin (Thermo Fisher Scientific, Cat. # 15-140-122), and 100µl per well was plated on top of the solidified matrices. Plates were harvested at desired time points and medium was replaced on remaining plates every 4 days. Cell viability in the harvested plates was assayed using the CellTiter Non-Radioactive Cell Proliferation Assay (Promega, Cat. # G4000) as per manufacturer's instructions.

D2.OR and D2A1 cells were similarly cultured in 18 well Glass Bottom chamber slides (ibidi, Cat. # 81817) for immunofluorescence with the following modifications - 20µl of the matrix was added per well and wells were solidified for 1h at 37°C following which 200 cells were added to each well.

RNA sequencing

MTB/TAN cells were cultured in vitro under dormancy conditions as described. Samples were harvested at baseline (D0), deinduction (8 h, D1, D3, D7, D14, D28), and reinduction (D7+, D14+, and D28+) timepoints. RNA isolation was performed using the RNeasy Mini kit (Qiagen, Cat. # 74106) and sequencing libraries were prepared using the TruSeq Stranded mRNA for NeoPrep kit (Illumina, Cat. # NP-202-1001). Sequencing was performed using 75-bp paired-end NextSeq (Illumina, Cat. # 20024907).

bioRxiv preprint doi: https://doi.org/10.1101/2023.01.31.526529; this version posted February 3, 2023. The copyright holder for this preprint (which was not certified by peer review) is the author/funder, who has granted bioRxiv a license to display the preprint in perpetuity. It is made available under aCC-BY-NC-ND 4.0 International license.

The quality of raw reads was assessed using FASTQC. Sequenced reads were mapped to the mm10 *Mus musculus* reference genome using Spliced Transcripts Alignment to a Reference (STAR). Gene-level read counts were determined using featureCounts. Principal component analysis (PCA) was performed using the top 1000 most variable genes assessed by per-gene standard deviations and was used to exclude distinct outliers from the downstream analysis. Read counts across samples were normalized and differentially expressed genes were identified using DESeq2.

Animal experiments

All animal studies were approved by the University of Pennsylvania Institutional Animal Care and Use Committee (IACUC). In vivo competition assays and recurrence-free survival assays were performed as previously described. Briefly, 1e06 cells (1:1 mixture of GFP^+ and $mCherry^+$ cells for competition assays or unmixed cells for recurrence-free survival assays and the CRISPR-Cas9 screen) were transplanted into the inguinal #4 mammary fat pads of *nu/nu* female mice (NCRNU-F, Taconic) and administered 2mg/ml doxycycline/5% sucrose via drinking water. Mice were de-induced by switching to regular drinking water once mammary tumors reached target size (5x5mm for competition assays; 3x3mm for recurrence-free survival assays and the CRISPR-Cas9 screen). Mice were palpated thrice a week and time-to-recurrence was assessed by Kaplan-Meier analysis. At the time of harvest, mice were administered 50mg/kg EdU (i.p.) 2h prior to euthanasia.

Plasmids and lentiviral production

LentiV_Cas9_puro (Addgene, Cat. # 108100) was used to generate Cas9 expressing *MTB/TAN*-derived primary tumor cells. LRG2.1 (Addgene, Cat. # 108098), LRG (Addgene, Cat. # 65656), or LRmCherry2.1 (Addgene, Cat. # 108099) vector backbones were utilized for cloning sgRNAs for CRISPR-Cas9 studies. For each sgRNA, sense and antisense oligos were

bioRxiv preprint doi: https://doi.org/10.1101/2023.01.31.526529; this version posted February 3, 2023. The copyright holder for this preprint (which was not certified by peer review) is the author/funder, who has granted bioRxiv a license to display the preprint in perpetuity. It is made available under aCC-BY-NC-ND 4.0 International license.

phosphorylated and annealed and then ligated into BsmB1-digested vector. Ligated vectors were transformed into the chemically competent Stbl3 bacteria (Thermo Fisher Scientific, Cat. # C737303). Successfully transformed bacterial clones were picked from Ampicillin selective plates and isolated DNA was sequenced using a U6 primer to confirm sgRNA incorporation.

Lentiviruses were generated in HEK293T cells using the TransIT-293 transfection reagent (Mirus, Cat. # MIR2700) to introduce packaging plasmids pMD2.G (Addgene, Cat. # 12259; 3µg) and psPAX2 (Addgene, Cat. # 12260; 6µg), and 9µg of the desired backbone containing the sgRNA of interest. sgRNA lentiviruses were titered by serial dilution in *MTB/TAN*-derived primary tumor cells using the fluorophore associated with the vector backbones as a readout by on the Attune NxT flow cytometry (Thermo Fisher).

CRISPR-Cas9 screen

Of the genes that were selectively enriched during dormancy in vitro that were encompassed by extracellular matrix-associated gene ontology terms, 95 genes were selected for CRISPR-Cas9 screening in vivo. In addition, positive control sgRNAs targeting genes that are known to be functional during disease progression (pro-proliferative and pro-survival genes) and negative control sgRNAs that are non-targeting were also included in this library. For the 95 genes, 4-5 sgRNAs were designed for each gene resulting in a total of 509 sgRNAs. Additionally, a size-matched library of non-targeting sgRNAs was prepared to aid data analysis.

sgRNAs were designed to target conserved functional domains that display low computationally predicted off-target scores using the GUIDES tool (http://guides.sanjanalab.org/), preferentially picking sgRNAs that have an A/T nucleotide at the 17th position of the sgRNA sequence. This approach maximizes functionally 'null' mutations and circumvents the need for subcloning the cells, thus maintaining their heterogeneity. These sgRNA oligo pools were cloned into the LRG expression vector following which the plasmid pool was amplified, purified, and packaged into lentiviruses. To ensure that *MTB/TAN*-Cas9 cells

bioRxiv preprint doi: https://doi.org/10.1101/2023.01.31.526529; this version posted February 3, 2023. The copyright holder for this preprint (which was not certified by peer review) is the author/funder, who has granted bioRxiv a license to display the preprint in perpetuity. It is made available under aCC-BY-NC-ND 4.0 International license.

receive only one sgRNA/cell, the lentiviral library was titered using the GFP selectable marker by flow cytometry (Attune NxT Thermo Fisher) and transduced at an MOI=0.3. Finally, the transduced cells were sorted (MoFlo Astrios, Beckman Coulter Life Sciences) and expanded prior to transplantation in vivo. All steps were performed such that each sgRNA was represented in >1500 cells/sgRNA to maintain coverage and improve the robustness of downstream analyses.

All samples harvested from mouse primary tumors and residual lesions were microdissected under a stereoscope and homogenized for genomic DNA extraction using the Quick-DNA Midiprep Plus kit (Zymo Research, Cat. # D4075). sgRNA inserts were amplified by PCR using the Phusion Flash High Fidelity PCR Master Mix (Thermo Fisher, Cat. # F548), followed by barcode and adapter addition. The libraries were then pooled, mixed with 5% PhiX (Thermo Fisher, Cat. # FC-110-3001) and massively parallel sequenced using the MiSeq reagent kit v3 150 cycle (Illumina, Cat. # MS-102-3001) on the MiSeq Instrument (Illumina).

Histology

When harvesting 3D assays for immunofluorescence, medium was aspirated and immediately fixed in 2% paraformaldehyde (Santa Cruz Biotechnology, Cat. # sc-281692) in PBS for 20 min at room temperature. Cells were then permeabilized in PBS containing 0.5% Triton X-100 for 10 min at room temperature. Wells were then rinsed three times in 1x PBS containing 100mM glycine before proceeding with the immunofluorescence protocol.

For in vitro immunofluorescence/labeling studies, *MTB/TAN*-derived primary tumor cells were cultured on glass coverslips (Bellco Glass Inc., Cat. # 1943-010015A) and treated with 5μM EdU for 2h before harvest. Coverslips containing cells were fixed in 4% paraformaldehyde for 15 min at room temperature. Cells were then permeabilized in PBS containing 0.5% Triton X-100 for 20 min at room temperature followed by wash steps in 3% bovine serum albumin in 1x PBS before proceeding with the immunofluorescence protocol.

bioRxiv preprint doi: https://doi.org/10.1101/2023.01.31.526529; this version posted February 3, 2023. The copyright holder for this preprint (which was not certified by peer review) is the author/funder, who has granted bioRxiv a license to display the preprint in perpetuity. It is made available under aCC-BY-NC-ND 4.0 International license.

For in vivo immunofluorescence/labeling studies, inguinal #4 mammary fat pads containing primary tumors, residual lesions, or recurrent tumors were dissected and fixed overnight in 4% paraformaldehyde overnight at 4°C. Samples were thoroughly washed and dehydrated prior to paraffin embedding and sectioning at 5µm. Slides were prepared by serial deparaffinization and rehydration followed by PBS washes and antigen retrieval in R-Buffer A (Electron Microscopy Sciences, Cat. # 62706-10) or R-Buffer B (Electron Microscopy Sciences, Cat. # 62706-11) using a retriever (Aptum, Cat. # RR2100-EU).

For GAG immunofluorescence, specificity controls were included where tissue sections were treated with Chondroitinase ABC (Amsbio, Cat. # AMS.E1028-02; 10mU/µl at pH 8) or Heparin lyase (Amsbio, Cat. # AMS.HEP-ENZ III-S; 20mU/µl at pH 7) at 37°C for 1h prior to immunofluorescence.

For labeling studies using coverslips for EdU (Thermo Fisher Scientific, Cat. # C10640) or on tissues for EdU (Sigma Aldrich, Cat. # BCK647-IV-IM-S) or TUNEL (Thermo Fisher Scientific, Cat. # C10619) samples were processed as per manufacturer's instructions prior to immunofluorescence.

Immunofluorescence samples were blocked with 5% goat serum in 1x PBS with mouse-on-mouse block (Vector Laboratories, Cat. # BMK-2202), washed 3 times in 1x PBS and incubated overnight at 4°C with primary antibodies or matched isotype controls diluted in 5% goat serum in 1x PBS with mouse-on-mouse diluent (Vector Laboratories, Cat. # BMK-2202) as follows: Primary antibodies - Rat anti-Ki67 (Thermo Fisher Scientific, Cat. # 14-5698; 1:100), Rabbit anti-Her2 (Cell Signaling, Cat. # 2165; 1:100), Rabbit anti-cleaved Caspase-3 (Cell Signaling, Cat. # 9664; 1:250), Mouse anti-Chondroitin sulfate (Sigma, Cat. # SAB4200696), Mouse anti-Heparan sulfate (Amsbio, Cat. # 370225), Rabbit anti-GFP (Cell Signaling, Cat. # 2956; 1:200), and Mouse anti-GFP (Living Colors, Cat. # 632381; 1:250). Isotype controls - Rat IgG (Thermo Fisher Scientific, Cat. # 02-9602), Rabbit IgG (Thermo Fisher Scientific, Cat. # 02-6102), Mouse IgG2a kappa (Thermo Fisher Scientific, Cat. # 14-4724-82).

bioRxiv preprint doi: https://doi.org/10.1101/2023.01.31.526529; this version posted February 3, 2023. The copyright holder for this preprint (which was not certified by peer review) is the author/funder, who has granted bioRxiv a license to display the preprint in perpetuity. It is made available under aCC-BY-NC-ND 4.0 International license.

After performing 3 washes with 1x PBS, samples were incubated with secondary antibodies at 37°C for 1h as follows: Secondary antibodies - Goat anti-mouse IgG2a Alexa488 (Thermo Fisher Scientific, Cat. # A21131; 1:1000), Goat anti-rabbit IgG Alexa488 (Thermo Fisher Scientific, Cat. # A11034; 1:1000), Goat anti-rabbit IgG Alexa594 (Thermo Fisher Scientific, Cat. # A11012; 1:1000), Goat anti-rat IgG Alexa568 (Thermo Fisher Scientific, Cat. # A11077; 1:1000), Goat anti-mouse IgM Alexa568 (Abcam, Cat. # ab175702; 1:1000).

Following incubation with secondary antibodies, samples were washed 3 times with 1x PBS and incubated with 0.5µg/ml Hoechst 33258 for 10 min at room temperature for nuclear counter staining. Samples were mounted using ProLong gold (Thermo Fisher Scientific, Cat. # P36934) and imaged using a DM 5000B Automated Upright Microscope with a DFC350 FX monochrome digital camera (Leica Microsystems). Images were quantified using QuPath-0.3.0 open source software.

Droplet digital PCR

Microdissected lesions from the in vivo experiments or cells harvested from the in vitro dormancy experiment were processed for genomic DNA isolation using the Quick-DNA Midiprep Plus kit (Zymo Research, Cat. # D4075) kit, or the QIAamp DNA mini kit (Thermo Fisher, Cat. # 51304), respectively. To quantify the numbers of GFP^+ and $mCherry^+$ cells, 50ng of gnomic DNA/sample was added together with the ddPCR Supermix for Probes (Bio-Rad, Cat. # 1863025) and the probes of interest: GFP (Bio-Rad, Cat. # dCNS372378948), mCherry (Bio-Rad, Cat. # dCNS507694046), and the control ApoB (Bio-Rad, Cat. # dMmuCNS4075944696). Droplets were generated using the AutoDG system (Bio-Rad, Cat. # 1864101) followed by PCR under the following conditions: 95°C for 5 min; 40 cycles at 94°C for 30 sec and 60°C for 1 min; 98°C for 10 min. Droplets were analyzed using the QX200 Droplet Reader (Bio-Rad, Cat. # 1864003). Droplet-derived copy numbers were first normalized to ApoB numbers to normalize

bioRxiv preprint doi: https://doi.org/10.1101/2023.01.31.526529; this version posted February 3, 2023. The copyright holder for this preprint (which was not certified by peer review) is the author/funder, who has granted bioRxiv a license to display the preprint in perpetuity. It is made available under aCC-BY-NC-ND 4.0 International license.

input and then converted to cell numbers by using the average copy number derived from singly transduced cells.

Western blot

Western blots were performed as described using the following antibodies: β-Tubulin (BioGenex, Cat. # MU122). Secondary antibodies used were anti-mouse 680LT (LI-COR Biosciences 925-68020), anti-rabbit 800CW (LI-COR Biosciences, Cat. # 925-32211),and anti-rat 800CW (LI-COR Biosciences, Cat. # 925-32219). Fluorescent signals were detected using the Odyssey detection system (LI-COR Biosciences), and band intensities were quantified using the Image Studio Ver 2.0 software (LI-COR Biosciences).

Glycan reductive isotope labeling – mass spectrometry (GRIL-LC/MS)

MTB/TAN-derived primary tumor cells were cultured for an in vitro dormancy time course as previously described and harvested at baseline (D0), deinduction (D7, D28), and reinduction (D28+) time points. At the time of harvest, cells were kept on ice, thoroughly washed 2 times with ice cold 1x PBS, and gently scraped into 1x PBS. Cells were pelleted down at 1500 rpm and the pellets were flash frozen for further analysis.

GAG isolation and purification was performed by sonicating the cell pellet in ultrapure distilled water (Invitrogen, Cat. # 10977-015) containing measured amount of protease inhibitor cocktail SetIII, EDTA free (EMD Millipore, Cat. # 539134-1ml) followed by adding equal volume of 2X wash buffer (100mM NaOAc and 400mM NaCl; pH 6). Protein digestion was done using bacterial protease (Sigma, Cat. # P5147) at a concentration of 0.4mg/ml at 37°C overnight (16h). Samples were then loaded on to a Poly-Prep column (Bio-Rad, Cat. # 731-1550) packed with pre-equilibrated DEAE Sephacel gel (Sigma, Cat. # 16505). Columns were washed with 10 bed volume of wash buffer (50mM NaOAc containing 200mM NaCl; pH 6) and bound GAG were

bioRxiv preprint doi: https://doi.org/10.1101/2023.01.31.526529; this version posted February 3, 2023. The copyright holder for this preprint (which was not certified by peer review) is the author/funder, who has granted bioRxiv a license to display the preprint in perpetuity. It is made available under aCC-BY-NC-ND 4.0 International license.

eluted using elution buffer (50mM NaOAc containing 1M NaCl; pH 6). Eluted samples were then loaded on to a PD10 desalting column (GE Healthcare, Cat. # 17-0851-01) pre-washed with 10% ethanol. Desalted GAG samples in 10% ethanol were lyophilized and used for further analysis.

Lyophilized samples were resuspended in MilliQ water and distributed for enzymatic digestion of chondroitin sulfate and heparan sulfate at 37°C for 24h using 30mU of Chondroitinase ABC (Amsbio, Cat. # AMS.E1028-02) and 10mU of Heparinase I, II, III (Ibex, Cat. # PN 50-010; PN 50-011; PN 50-012 Heparinase I, II, and III), respectively. Digested samples were spin-filtered using a 3K MWCO spin filtering unit (Pall Life Sciences, Cat. # OD003C34) and tagged with $^{12}C_6$-aniline in the presence of a reducing agent 1M NaCNBr in a mixture of DMSO: HOAc (65:35 v/v). Reductive isotope labeling is performed at 65°C for 45 minutes, followed by incubation at 37°C for 16 h. Samples were mixed with internal standards ($^{13}C_6$-aniline tagged disaccharides from chondroitin sulfate and heparan sulfate respectively) and LC/MS is performed in negative mode using an LTQ-Orbitrap (Thermo Fisher Scientific) mass spectrometer.

Statistics

For each gene expression signature in each data set, signature scores were calculated as weighted averages of z-score transformed expression data across signature genes, where the z-score transformation was done for each gene across the samples, and the weights are 1 for genes expected to be positively associated with the signature target (e.g. dormancy) and -1 for genes expected to be negatively associated with the signature target.

CRISPR screen sequencing reads were de-convoluted using the unique barcodes associated with each sample and mapped to sgRNA sequences. The abundance of each sgRNA was normalized by the median of ratios (MoR, as implemented in DESeq2), the total read count (T, as % of total), the robust z-score (RZ, with median-centering and MAD-scaling),

bioRxiv preprint doi: https://doi.org/10.1101/2023.01.31.526529; this version posted February 3, 2023. The copyright holder for this preprint (which was not certified by peer review) is the author/funder, who has granted bioRxiv a license to display the preprint in perpetuity. It is made available under aCC-BY-NC-ND 4.0 International license.

trimmed mean of M-values (TMM, as implemented in edgeR), and normalized rank (NR, as percentile rank) following which depletion and enrichment scores for each sgRNA were calculated by MAGeCK or the Mann-Whitney U test followed by robust rank aggregation (RRA). False positive rates were controlled for using data from the size matched non-targeting negative control (NC) sgRNA library. In addition to the five normalization methods above, an NC-centric version of MoR was done using negative control gRNAs to calculate scaling factors instead of using all gRNAs, and an NC-centric version of RZ was done using the median and MAD values calculated from negative control gRNAs instead of all gRNAs. Methods with the highest sensitivity were as follows: MAGeCK-RRA-M, MAGeCK-RRA-T, MW-RRA-MoR, MW-RRA-NC_MoR, MW-RRA-NC_RZ, MW-RRA-NR, MW-RRA-RZ, MW-RRA-TMM. Using *p* values from the 8 tests above, hits called by a larger number of tests were prioritized for further validation.

To determine differences between multiple groups, ANOVA followed by Tukey's multiple comparisons test was used. In cases where the data were not normally distributed, the Mann-Whitney U test was used to determine statistical significance. Survival curves were subjected to Kaplan-Meier analysis and *p* values and hazard ratios were calculated using the Mantel-Haenszel method.

bioRxiv preprint doi: https://doi.org/10.1101/2023.01.31.526529; this version posted February 3, 2023. The copyright holder for this preprint (which was not certified by peer review) is the author/funder, who has granted bioRxiv a license to display the preprint in perpetuity. It is made available under aCC-BY-NC-ND 4.0 International license.

References

1. Sung, H., Ferlay, J., Siegel, R.L., Laversanne, M., Soerjomataram, I., Jemal, A., and Bray, F. (2021). Global Cancer Statistics 2020: GLOBOCAN Estimates of Incidence and Mortality Worldwide for 36 Cancers in 185 Countries. CA Cancer J Clin *71*, 209-249. 10.3322/caac.21660.
2. Pan, H., Gray, R., Braybrooke, J., Davies, C., Taylor, C., McGale, P., Peto, R., Pritchard, K.I., Bergh, J., Dowsett, M., et al. (2017). 20-Year Risks of Breast-Cancer Recurrence after Stopping Endocrine Therapy at 5 Years. N Engl J Med *377*, 1836-1846. 10.1056/NEJMoa1701830.
3. Pedersen, R.N., Esen, B.O., Mellemkjaer, L., Christiansen, P., Ejlertsen, B., Lash, T.L., Norgaard, M., and Cronin-Fenton, D. (2021). The Incidence of Breast Cancer Recurrence 10-32 Years after Primary Diagnosis. J Natl Cancer Inst. 10.1093/jnci/djab202.
4. Pantel, K., Schlimok, G., Braun, S., Kutter, D., Lindemann, F., Schaller, G., Funke, I., Izbicki, J.R., and Riethmuller, G. (1993). Differential expression of proliferation-associated molecules in individual micrometastatic carcinoma cells. J Natl Cancer Inst *85*, 1419-1424. 10.1093/jnci/85.17.1419.
5. Moody, S.E., Sarkisian, C.J., Hahn, K.T., Gunther, E.J., Pickup, S., Dugan, K.D., Innocent, N., Cardiff, R.D., Schnall, M.D., and Chodosh, L.A. (2002). Conditional activation of Neu in the mammary epithelium of transgenic mice results in reversible pulmonary metastasis. Cancer Cell *2*, 451-461. 10.1016/s1535-6108(02)00212-x.
6. Ruth, J.R., Pant, D.K., Pan, T.C., Seidel, H.E., Baksh, S.C., Keister, B.A., Singh, R., Sterner, C.J., Bakewell, S.J., Moody, S.E., et al. (2021). Cellular dormancy in minimal residual disease following targeted therapy. Breast Cancer Res *23*, 63. 10.1186/s13058-021-01416-9.
7. Gunther, E.J., Moody, S.E., Belka, G.K., Hahn, K.T., Innocent, N., Dugan, K.D., Cardiff, R.D., and Chodosh, L.A. (2003). Impact of p53 loss on reversal and recurrence of conditional Wnt-induced tumorigenesis. Genes Dev *17*, 488-501. 10.1101/gad.1051603.
8. Janghorban, M., Yang, Y., Zhao, N., Hamor, C., Nguyen, T.M., Zhang, X.H., and Rosen, J.M. (2021). Single Cell Analysis Unveils the Role of the Tumor Immune Microenvironment and Notch Signaling in Dormant Minimal Residual Disease. Cancer Res. 10.1158/0008-5472.CAN-21-1230.
9. Morris, V.L., Tuck, A.B., Wilson, S.M., Percy, D., and Chambers, A.F. (1993). Tumor progression and metastasis in murine D2 hyperplastic alveolar nodule mammary tumor cell lines. Clin Exp Metastasis *11*, 103-112. 10.1007/BF00880071.
10. Morris, V.L., Koop, S., MacDonald, I.C., Schmidt, E.E., Grattan, M., Percy, D., Chambers, A.F., and Groom, A.C. (1994). Mammary carcinoma cell lines of high and low metastatic potential differ not in extravasation but in subsequent migration and growth. Clin Exp Metastasis *12*, 357-367. 10.1007/BF01755879.
11. Naumov, G.N., MacDonald, I.C., Weinmeister, P.M., Kerkvliet, N., Nadkarni, K.V., Wilson, S.M., Morris, V.L., Groom, A.C., and Chambers, A.F. (2002). Persistence of solitary mammary carcinoma cells in a secondary site: a possible contributor to dormancy. Cancer Res *62*, 2162-2168.
12. Ren, Q., Khoo, W.H., Corr, A.P., Phan, T.G., Croucher, P.I., and Stewart, S.A. (2022). Gene expression predicts dormant metastatic breast cancer cell phenotype. Breast Cancer Res *24*, 10. 10.1186/s13058-022-01503-5.
13. Ghajar, C.M., Peinado, H., Mori, H., Matei, I.R., Evason, K.J., Brazier, H., Almeida, D., Koller, A., Hajjar, K.A., Stainier, D.Y., et al. (2013). The perivascular niche regulates breast tumour dormancy. Nat Cell Biol *15*, 807-817. 10.1038/ncb2767.

bioRxiv preprint doi: https://doi.org/10.1101/2023.01.31.526529; this version posted February 3, 2023. The copyright holder for this preprint (which was not certified by peer review) is the author/funder, who has granted bioRxiv a license to display the preprint in perpetuity. It is made available under aCC-BY-NC-ND 4.0 International license.

14. Dai, J., Cimino, P.J., Gouin, K.H., 3rd, Grzelak, C.A., Barrett, A., Lim, A.R., Long, A., Weaver, S., Saldin, L.T., Uzamere, A., et al. (2022). Astrocytic laminin-211 drives disseminated breast tumor cell dormancy in brain. Nat Cancer *3*, 25-42. 10.1038/s43018-021-00297-3.
15. Albrengues, J., Shields, M.A., Ng, D., Park, C.G., Ambrico, A., Poindexter, M.E., Upadhyay, P., Uyeminami, D.L., Pommier, A., Küttner, V., et al. (2018). Neutrophil extracellular traps produced during inflammation awaken dormant cancer cells in mice. Science. 10.1126/science.aao4227.
16. Barkan, D., Kleinman, H., Simmons, J.L., Asmussen, H., Kamaraju, A.K., Hoenorhoff, M.J., Liu, Z.Y., Costes, S.V., Cho, E.H., Lockett, S., et al. (2008). Inhibition of metastatic outgrowth from single dormant tumor cells by targeting the cytoskeleton. Cancer Res *68*, 6241-6250. 10.1158/0008-5472.CAN-07-6849.
17. Korah, R., Boots, M., and Wieder, R. (2004). Integrin alpha5beta1 promotes survival of growth-arrested breast cancer cells: an in vitro paradigm for breast cancer dormancy in bone marrow. Cancer Res *64*, 4514-4522. 10.1158/0008-5472.CAN-03-3853.
18. Aguirre-Ghiso, J.A., Liu, D., Mignatti, A., Kovalski, K., and Ossowski, L. (2001). Urokinase receptor and fibronectin regulate the ERK(MAPK) to p38(MAPK) activity ratios that determine carcinoma cell proliferation or dormancy in vivo. Mol Biol Cell *12*, 863-879. 10.1091/mbc.12.4.863.
19. Barney, L.E., Hall, C.L., Schwartz, A.D., Parks, A.N., Sparages, C., Galarza, S., Platt, M.O., Mercurio, A.M., and Peyton, S.R. (2020). Tumor cell-organized fibronectin maintenance of a dormant breast cancer population. Sci Adv *6*, eaaz4157. 10.1126/sciadv.aaz4157.
20. Barkan, D., El Touny, L.H., Michalowski, A.M., Smith, J.A., Chu, I., Davis, A.S., Webster, J.D., Hoover, S., Simpson, R.M., Gauldie, J., and Green, J.E. (2010). Metastatic growth from dormant cells induced by a col-I-enriched fibrotic environment. Cancer Res *70*, 5706-5716. 10.1158/0008-5472.CAN-09-2356.
21. Gao, H., Chakraborty, G., Zhang, Z., Akalay, I., Gadiya, M., Gao, Y., Sinha, S., Hu, J., Jiang, C., Akram, M., et al. (2016). Multi-organ Site Metastatic Reactivation Mediated by Non-canonical Discoidin Domain Receptor 1 Signaling. Cell *166*, 47-62. 10.1016/j.cell.2016.06.009.
22. Di Martino, J.S., Nobre, A.R., Mondal, C., Taha, I., Farias, E.F., Fertig, E.J., Naba, A., Aguirre-Ghiso, J.A., and Bravo-Cordero, J.J. (2022). A tumor-derived type III collagen-rich ECM niche regulates tumor cell dormancy. Nature cancer *3*, 90-107. 10.1038/s43018-021-00291-9.
23. Merry, C.L.R., Lindahl, U., Couchman, J., and Esko, J.D. (2022). Proteoglycans and Sulfated Glycosaminoglycans. In Essentials of Glycobiology, th, A. Varki, R.D. Cummings, J.D. Esko, P. Stanley, G.W. Hart, M. Aebi, D. Mohnen, T. Kinoshita, N.H. Packer, et al., eds. pp. 217-232. 10.1101/glycobiology.4e.17.
24. Iozzo, R.V., and Schaefer, L. (2015). Proteoglycan form and function: A comprehensive nomenclature of proteoglycans. Matrix Biol *42*, 11-55. 10.1016/j.matbio.2015.02.003.
25. Couchman, J.R., and Pataki, C.A. (2012). An introduction to proteoglycans and their localization. J Histochem Cytochem *60*, 885-897. 10.1369/0022155412464638.
26. Bishop, J.R., Schuksz, M., and Esko, J.D. (2007). Heparan sulphate proteoglycans fine-tune mammalian physiology. Nature *446*, 1030-1037. 10.1038/nature05817.
27. Esko, J.D., and Selleck, S.B. (2002). Order out of chaos: assembly of ligand binding sites in heparan sulfate. Annu Rev Biochem *71*, 435-471. 10.1146/annurev.biochem.71.110601.135458.
28. Bai, X., Zhou, D., Brown, J.R., Crawford, B.E., Hennet, T., and Esko, J.D. (2001). Biosynthesis of the linkage region of glycosaminoglycans: cloning and activity of

bioRxiv preprint doi: https://doi.org/10.1101/2023.01.31.526529; this version posted February 3, 2023. The copyright holder for this preprint (which was not certified by peer review) is the author/funder, who has granted bioRxiv a license to display the preprint in perpetuity. It is made available under aCC-BY-NC-ND 4.0 International license.

galactosyltransferase II, the sixth member of the beta 1,3-galactosyltransferase family (beta 3GalT6). J Biol Chem *276*, 48189-48195. 10.1074/jbc.M107339200.

29. Malfait, F., Kariminejad, A., Van Damme, T., Gauche, C., Syx, D., Merhi-Soussi, F., Gulberti, S., Symoens, S., Vanhauwaert, S., Willaert, A., et al. (2013). Defective initiation of glycosaminoglycan synthesis due to B3GALT6 mutations causes a pleiotropic Ehlers-Danlos-syndrome-like connective tissue disorder. Am J Hum Genet *92*, 935-945. 10.1016/j.ajhg.2013.04.016.
30. Ben-Mahmoud, A., Ben-Salem, S., Al-Sorkhy, M., John, A., Ali, B.R., and Al-Gazali, L. (2018). A B3GALT6 variant in patient originally described as Al-Gazali syndrome and implicating the endoplasmic reticulum quality control in the mechanism of some beta3GalT6-pathy mutations. Clin Genet *93*, 1148-1158. 10.1111/cge.13236.
31. Nakajima, M., Mizumoto, S., Miyake, N., Kogawa, R., Iida, A., Ito, H., Kitoh, H., Hirayama, A., Mitsubuchi, H., Miyazaki, O., et al. (2013). Mutations in B3GALT6, which encodes a glycosaminoglycan linker region enzyme, cause a spectrum of skeletal and connective tissue disorders. Am J Hum Genet *92*, 927-934. 10.1016/j.ajhg.2013.04.003.
32. Alvarez, J.V., Pan, T.C., Ruth, J., Feng, Y., Zhou, A., Pant, D., Grimley, J.S., Wandless, T.J., Demichele, A., Investigators, I.S.T., and Chodosh, L.A. (2013). Par-4 downregulation promotes breast cancer recurrence by preventing multinucleation following targeted therapy. Cancer Cell *24*, 30-44. 10.1016/j.ccr.2013.05.007.
33. Feng, Y., Pan, T.C., Pant, D.K., Chakrabarti, K.R., Alvarez, J.V., Ruth, J.R., and Chodosh, L.A. (2014). SPSB1 promotes breast cancer recurrence by potentiating c-MET signaling. Cancer Discov *4*, 790-803. 10.1158/2159-8290.CD-13-0548.
34. Payne, A.W., Pant, D.K., Pan, T.C., and Chodosh, L.A. (2014). Ceramide kinase promotes tumor cell survival and mammary tumor recurrence. Cancer Res *74*, 6352-6363. 10.1158/0008-5472.CAN-14-1292.
35. D'Cruz, C.M., Gunther, E.J., Boxer, R.B., Hartman, J.L., Sintasath, L., Moody, S.E., Cox, J.D., Ha, S.I., Belka, G.K., Golant, A., et al. (2001). c-MYC induces mammary tumorigenesis by means of a preferred pathway involving spontaneous Kras2 mutations. Nat Med *7*, 235-239. 10.1038/84691.
36. Gunther, E.J., Belka, G.K., Wertheim, G.B., Wang, J., Hartman, J.L., Boxer, R.B., and Chodosh, L.A. (2002). A novel doxycycline-inducible system for the transgenic analysis of mammary gland biology. FASEB J *16*, 283-292. 10.1096/fj.01-0551com.
37. Alvarez, J.V., Belka, G.K., Pan, T.C., Chen, C.C., Blankemeyer, E., Alavi, A., Karp, J.S., and Chodosh, L.A. (2014). Oncogene pathway activation in mammary tumors dictates FDG-PET uptake. Cancer Res *74*, 7583-7598. 10.1158/0008-5472.CAN-14-1235.
38. Abravanel, D.L., Belka, G.K., Pan, T.C., Pant, D.K., Collins, M.A., Sterner, C.J., and Chodosh, L.A. (2015). Notch promotes recurrence of dormant tumor cells following HER2/neu-targeted therapy. J Clin Invest *125*, 2484-2496. 10.1172/JCI74883.
39. Stickeler, E., Pils, D., Klar, M., Orlowsk-Volk, M., Zur Hausen, A., Jager, M., Watermann, D., Gitsch, G., Zeillinger, R., and Tempfer, C.B. (2011). Basal-like molecular subtype and HER4 up-regulation and response to neoadjuvant chemotherapy in breast cancer. Oncol Rep *26*, 1037-1045. 10.3892/or.2011.1392.
40. Turnbull, A.K., Arthur, L.M., Renshaw, L., Larionov, A.A., Kay, C., Dunbier, A.K., Thomas, J.S., Dowsett, M., Sims, A.H., and Dixon, J.M. (2015). Accurate Prediction and Validation of Response to Endocrine Therapy in Breast Cancer. J Clin Oncol *33*, 2270-2278. 10.1200/JCO.2014.57.8963.
41. Arthur, L.M., Turnbull, A.K., Webber, V.L., Larionov, A.A., Renshaw, L., Kay, C., Thomas, J.S., Dixon, J.M., and Sims, A.H. (2014). Molecular changes in lobular breast cancers in response to endocrine therapy. Cancer Res *74*, 5371-5376. 10.1158/0008-5472.CAN-14-0620.

bioRxiv preprint doi: https://doi.org/10.1101/2023.01.31.526529; this version posted February 3, 2023. The copyright holder for this preprint (which was not certified by peer review) is the author/funder, who has granted bioRxiv a license to display the preprint in perpetuity. It is made available under aCC-BY-NC-ND 4.0 International license.

42. Miller, W.R., Larionov, A.A., Renshaw, L., Anderson, T.J., White, S., Murray, J., Murray, E., Hampton, G., Walker, J.R., Ho, S., et al. (2007). Changes in breast cancer transcriptional profiles after treatment with the aromatase inhibitor, letrozole. Pharmacogenet Genomics *17*, 813-826. 10.1097/FPC.0b013e32820b853a.
43. Korde, L.A., Lusa, L., McShane, L., Lebowitz, P.F., Lukes, L., Camphausen, K., Parker, J.S., Swain, S.M., Hunter, K., and Zujewski, J.A. (2010). Gene expression pathway analysis to predict response to neoadjuvant docetaxel and capecitabine for breast cancer. Breast Cancer Res Treat *119*, 685-699. 10.1007/s10549-009-0651-3.
44. Gruosso, T., Mieulet, V., Cardon, M., Bourachot, B., Kieffer, Y., Devun, F., Dubois, T., Dutreix, M., Vincent-Salomon, A., Miller, K.M., and Mechta-Grigoriou, F. (2016). Chronic oxidative stress promotes H2AX protein degradation and enhances chemosensitivity in breast cancer patients. EMBO Mol Med *8*, 527-549. 10.15252/emmm.201505891.
45. Gonzalez-Angulo, A.M., Iwamoto, T., Liu, S., Chen, H., Do, K.A., Hortobagyi, G.N., Mills, G.B., Meric-Bernstam, F., Symmans, W.F., and Pusztai, L. (2012). Gene expression, molecular class changes, and pathway analysis after neoadjuvant systemic therapy for breast cancer. Clin Cancer Res *18*, 1109-1119. 10.1158/1078-0432.CCR-11-2762.
46. Delbaere, S., De Clercq, A., Mizumoto, S., Noborn, F., Bek, J.W., Alluyn, L., Gistelinck, C., Syx, D., Salmon, P.L., Coucke, P.J., et al. (2020). b3galt6 Knock-Out Zebrafish Recapitulate beta3GalT6-Deficiency Disorders in Human and Reveal a Trisaccharide Proteoglycan Linkage Region. Front Cell Dev Biol *8*, 597857. 10.3389/fcell.2020.597857.
47. Conant, D., Hsiau, T., Rossi, N., Oki, J., Maures, T., Waite, K., Yang, J., Joshi, S., Kelso, R., Holden, K., et al. (2022). Inference of CRISPR Edits from Sanger Trace Data. CRISPR J *5*, 123-130. 10.1089/crispr.2021.0113.
48. Prunier, C., Alay, A., van Dijk, M., Ammerlaan, K.L., van Gelderen, S., Marvin, D.L., Teunisse, A., Slieker, R.C., Szuhai, K., Jochemsen, A.G., et al. (2021). Breast cancer dormancy is associated with a 4NG1 state and not senescence. NPJ Breast Cancer *7*, 140. 10.1038/s41523-021-00347-0.
49. Prydz, K., and Dalen, K.T. (2000). Synthesis and sorting of proteoglycans. J Cell Sci *113 Pt 2*, 193-205.
50. Rapraeger, A.C., Krufka, A., and Olwin, B.B. (1991). Requirement of heparan sulfate for bFGF-mediated fibroblast growth and myoblast differentiation. Science *252*, 1705-1708. 10.1126/science.1646484.
51. Johnson, C.E., Crawford, B.E., Stavridis, M., Ten Dam, G., Wat, A.L., Rushton, G., Ward, C.M., Wilson, V., van Kuppevelt, T.H., Esko, J.D., et al. (2007). Essential alterations of heparan sulfate during the differentiation of embryonic stem cells to Sox1-enhanced green fluorescent protein-expressing neural progenitor cells. Stem Cells *25*, 1913-1923. 10.1634/stemcells.2006-0445.
52. Ashikari-Hada, S., Habuchi, H., Sugaya, N., Kobayashi, T., and Kimata, K. (2009). Specific inhibition of FGF-2 signaling with 2-O-sulfated octasaccharides of heparan sulfate. Glycobiology *19*, 644-654. 10.1093/glycob/cwp031.
53. Marques, C., Reis, C.A., Vives, R.R., and Magalhaes, A. (2021). Heparan Sulfate Biosynthesis and Sulfation Profiles as Modulators of Cancer Signalling and Progression. Front Oncol *11*, 778752. 10.3389/fonc.2021.778752.
54. Lawrence, R., Olson, S.K., Steele, R.E., Wang, L., Warrior, R., Cummings, R.D., and Esko, J.D. (2008). Evolutionary differences in glycosaminoglycan fine structure detected by quantitative glycan reductive isotope labeling. J Biol Chem *283*, 33674-33684. 10.1074/jbc.M804288200.
55. Lawrence, R., Lu, H., Rosenberg, R.D., Esko, J.D., and Zhang, L. (2008). Disaccharide structure code for the easy representation of constituent oligosaccharides from glycosaminoglycans. Nat Methods *5*, 291-292. 10.1038/nmeth0408-291.

bioRxiv preprint doi: https://doi.org/10.1101/2023.01.31.526529; this version posted February 3, 2023. The copyright holder for this preprint (which was not certified by peer review) is the author/funder, who has granted bioRxiv a license to display the preprint in perpetuity. It is made available under aCC-BY-NC-ND 4.0 International license.

56. Sugaya, N., Habuchi, H., Nagai, N., Ashikari-Hada, S., and Kimata, K. (2008). 6-O-sulfation of heparan sulfate differentially regulates various fibroblast growth factor-dependent signalings in culture. J Biol Chem *283*, 10366-10376. 10.1074/jbc.M705948200.
57. Qiu, H., Shi, S., Yue, J., Xin, M., Nairn, A.V., Lin, L., Liu, X., Li, G., Archer-Hartmann, S.A., Dela Rosa, M., et al. (2018). A mutant-cell library for systematic analysis of heparan sulfate structure-function relationships. Nat Methods *15*, 889-899. 10.1038/s41592-018-0189-6.
58. Ornitz, D.M., and Itoh, N. (2015). The Fibroblast Growth Factor signaling pathway. Wiley Interdiscip Rev Dev Biol *4*, 215-266. 10.1002/wdev.176.
59. Weiss, R.J., Spahn, P.N., Chiang, A.W.T., Liu, Q., Li, J., Hamill, K.M., Rother, S., Clausen, T.M., Hoeksema, M.A., Timm, B.M., et al. (2021). Genome-wide screens uncover KDM2B as a modifier of protein binding to heparan sulfate. Nat Chem Biol *17*, 684-692. 10.1038/s41589-021-00776-9.
60. Huang, M.L., Smith, R.A., Trieger, G.W., and Godula, K. (2014). Glycocalyx remodeling with proteoglycan mimetics promotes neural specification in embryonic stem cells. J Am Chem Soc *136*, 10565-10568. 10.1021/ja505012a.
61. Bayne, L.J., Nivar, I., Goodspeed, B., Deluca, S.E., Wileyto, P., Shih, N.N.C., Nayak, A., Feldman, M.D., Edwards, J., Fox, K., et al. (2021). Identifying breast cancer survivors with dormant disseminated tumor cells: The PENN-SURMOUNT screening study [abstract]. Cancer Res *81* (*4*).
62. Bayne, L.J., Nivar, I., Goodspeed, B., Wileyto, P., Savage, J., Shih, N.N.C., Feldman, M.D., Edwards, J., Clark, A.S., Fox, K.R., et al. (2018). Detection and targeting of minimal residual disease in breast cancer to reduce recurrence: The PENN-SURMOUNT and CLEVER trials [abstract]. Cancer Res *78* (*4*).
63. Hassan, N., Greve, B., Espinoza-Sanchez, N.A., and Gotte, M. (2021). Cell-surface heparan sulfate proteoglycans as multifunctional integrators of signaling in cancer. Cell Signal *77*, 109822. 10.1016/j.cellsig.2020.109822.
64. Shibue, T., Reinhardt, F., and Weinberg, R.A. (2019). Syndecan-Mediated Ligation of ECM Proteins Triggers Proliferative Arrest of Disseminated Tumor Cells. Cancer Res *79*, 5944-5957. 10.1158/0008-5472.CAN-19-1165.
65. Dieter, S.M., Lovecchio, D., Pataskar, A., Zowada, M.K., Korner, P.R., Khalizieva, A., van Tellingen, O., Jager, D., Glimm, H., and Agami, R. (2022). Suppression of heparan sulfation re-sensitizes YAP1-driven melanoma to MAPK pathway inhibitors. Oncogene *41*, 3953-3968. 10.1038/s41388-022-02400-z.
66. Turner, N., and Grose, R. (2010). Fibroblast growth factor signalling: from development to cancer. Nat Rev Cancer *10*, 116-129. 10.1038/nrc2780.
67. Bado, I.L., Zhang, W., Hu, J., Xu, Z., Wang, H., Sarkar, P., Li, L., Wan, Y.W., Liu, J., Wu, W., et al. (2021). The bone microenvironment increases phenotypic plasticity of ER(+) breast cancer cells. Dev Cell *56*, 1100-1117 e1109. 10.1016/j.devcel.2021.03.008.
68. Barrios, J., and Wieder, R. (2009). Dual FGF-2 and intergrin alpha5beta1 signaling mediate GRAF-induced RhoA inactivation in a model of breast cancer dormancy. Cancer Microenviron *2*, 33-47. 10.1007/s12307-009-0019-6.
69. Nobre, A.R., Dalla, E., Yang, J., Huang, X., Wullkopf, L., Risson, E., Razghandi, P., Anton, M.L., Zheng, W., Seoane, J.A., et al. (2022). ZFP281 drives a mesenchymal-like dormancy program in early disseminated breast cancer cells that prevents metastatic outgrowth in the lung. Nat Cancer. 10.1038/s43018-022-00424-8.
70. Schram, A.M., Kamath, S.D., El-Khoueiry, A.B., Borad, M.J., Mody, K., Mahipal, A., Goyal, L., Sahai, V., Schmidt-Kittler, O., Shen, J., et al. (2021). First-in-human study of highly selective FGFR2 inhibitor, RLY-4008, in patients with intrahepatic cholangiocarcinoma and other advanced solid tumors. Journal of clinical oncology :

bioRxiv preprint doi: https://doi.org/10.1101/2023.01.31.526529; this version posted February 3, 2023. The copyright holder for this preprint (which was not certified by peer review) is the author/funder, who has granted bioRxiv a license to display the preprint in perpetuity. It is made available under aCC-BY-NC-ND 4.0 International license.

official journal of the American Society of Clinical Oncology. 10.1200/JCO.2021.39.15_suppl.TPS4165 Journal of Clinical Oncology 39, no. 15_suppl.

71. Statsenko, G., Fedyanin, M., Moiseyenko, V., Vladimirova, L.Y., Tsimafeyeu, I., and Tjulandin, S. (2020). A phase Ib study of alofanib, an allosteric FGFR2 inhibitor, in patients with advanced or metastatic gastric cancer. 10.1200/JCO.2020.38.4_suppl.TPS466 Journal of Clinical Oncology 38, no. 4_suppl.

72. Corti, F., Wang, Y., Rhodes, J.M., Atri, D., Archer-Hartmann, S., Zhang, J., Zhuang, Z.W., Chen, D., Wang, T., Wang, Z., et al. (2019). N-terminal syndecan-2 domain selectively enhances 6-O heparan sulfate chains sulfation and promotes VEGFA165-dependent neovascularization. Nat Commun *10*, 1562. 10.1038/s41467-019-09605-z.

73. Langford, J.K., Stanley, M.J., Cao, D., and Sanderson, R.D. (1998). Multiple heparan sulfate chains are required for optimal syndecan-1 function. J Biol Chem *273*, 29965-29971. 10.1074/jbc.273.45.29965.

74. Critcher, M., and Huang, M.L. (2022). Excavating proteoglycan structure-function relationships: modern approaches to capture the interactions of ancient biomolecules. Am J Physiol Cell Physiol *323*, C415-C422. 10.1152/ajpcell.00222.2022.

bioRxiv preprint doi: https://doi.org/10.1101/2023.01.31.526529; this version posted February 3, 2023. The copyright holder for this preprint (which was not certified by peer review) is the author/funder, who has granted bioRxiv a license to display the preprint in perpetuity. It is made available under aCC-BY-NC-ND 4.0 International license.

Figure 1

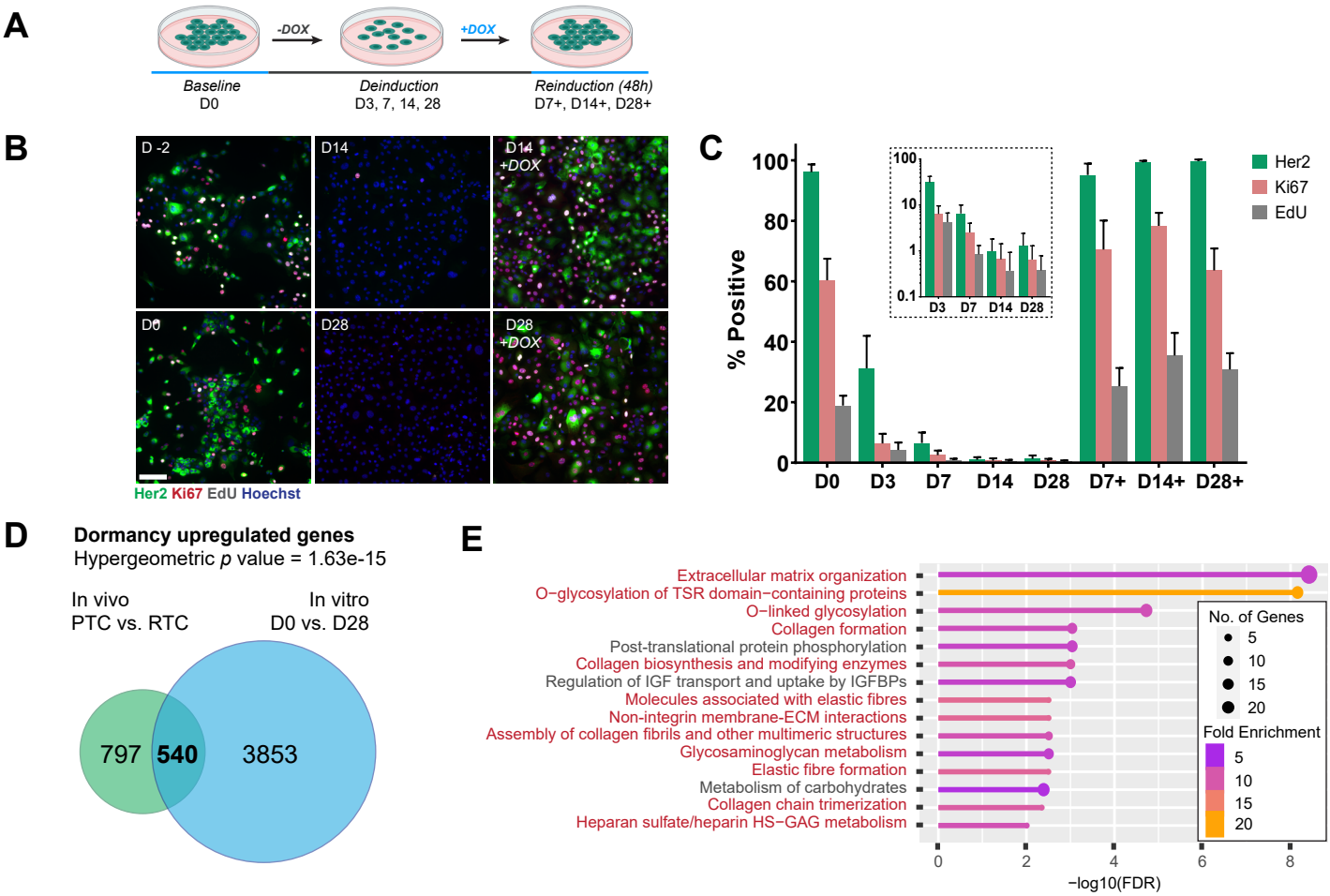

N	Time point	Effect size	p-value	Treatment
21	Surgery	**0.59**	**0.013**	Mixed (anthracycline/taxane/trastuzumab)
7	Surgery	0.23	0.56	4 cycles of epirubicin +cyclophosphamide, 4 cycles of taxanes
14	Post-Tx	**0.73**	**0.017**	1 cycle of docetaxel + capecitabine
16	Surgery	0.39	0.14	4 cycles of docetaxel + capecitabine
58	Post-Tx	**1.21**	**7.2e-13**	2 weeks on letrozole
35	Post-Tx_1	**1.05**	**4.3e-07**	2 weeks on letrozole
38	Post-Tx_2	**0.97**	**6.8e-07**	3 months on letrozole
25	Post-Tx	**0.98**	**5.4e-05**	4 cycles of epirubicin + cyclophosphamide

Fig. 1: Dormant tumor cells display cell-autonomous upregulation of ECM-related transcripts following therapy
A. Experimental schematic indicating time points for in vitro dormancy (IVD) assay using *MTB/TAN* cells. **B.** Immunofluorescence for Her2 (green), Ki67 (red), and EdU (grey) with Hoechst nuclear staining (blue) during IVD. **C.** Quantification of (**B**) represented as mean ± standard deviation (SD). Inset displays the percentages at deinduction time points on a $\log_{10}$ y-axis. Scale bar=100μm. **D.** Hypergeometric test and Venn diagram depicting the overlap between the in vivo and IVD-derived upregulated gene set. **E.** Top 15 Reactome gene ontology terms for the overlapping upregulated gene set. ECM-associated categories highlighted in red. **F.** Core RTC signature enrichment following neoadjuvant therapies vs. pre-treatment (pre-tx) samples across 6 patient datasets measured by effect size (mean of pair-wise difference in signature scores). Significant effects are highlighted in pink.

bioRxiv preprint doi: https://doi.org/10.1101/2023.01.31.526529; this version posted February 3, 2023. The copyright holder for this preprint (which was not certified by peer review) is the author/funder, who has granted bioRxiv a license to display the preprint in perpetuity. It is made available under aCC-BY-NC-ND 4.0 International license.

Figure 2

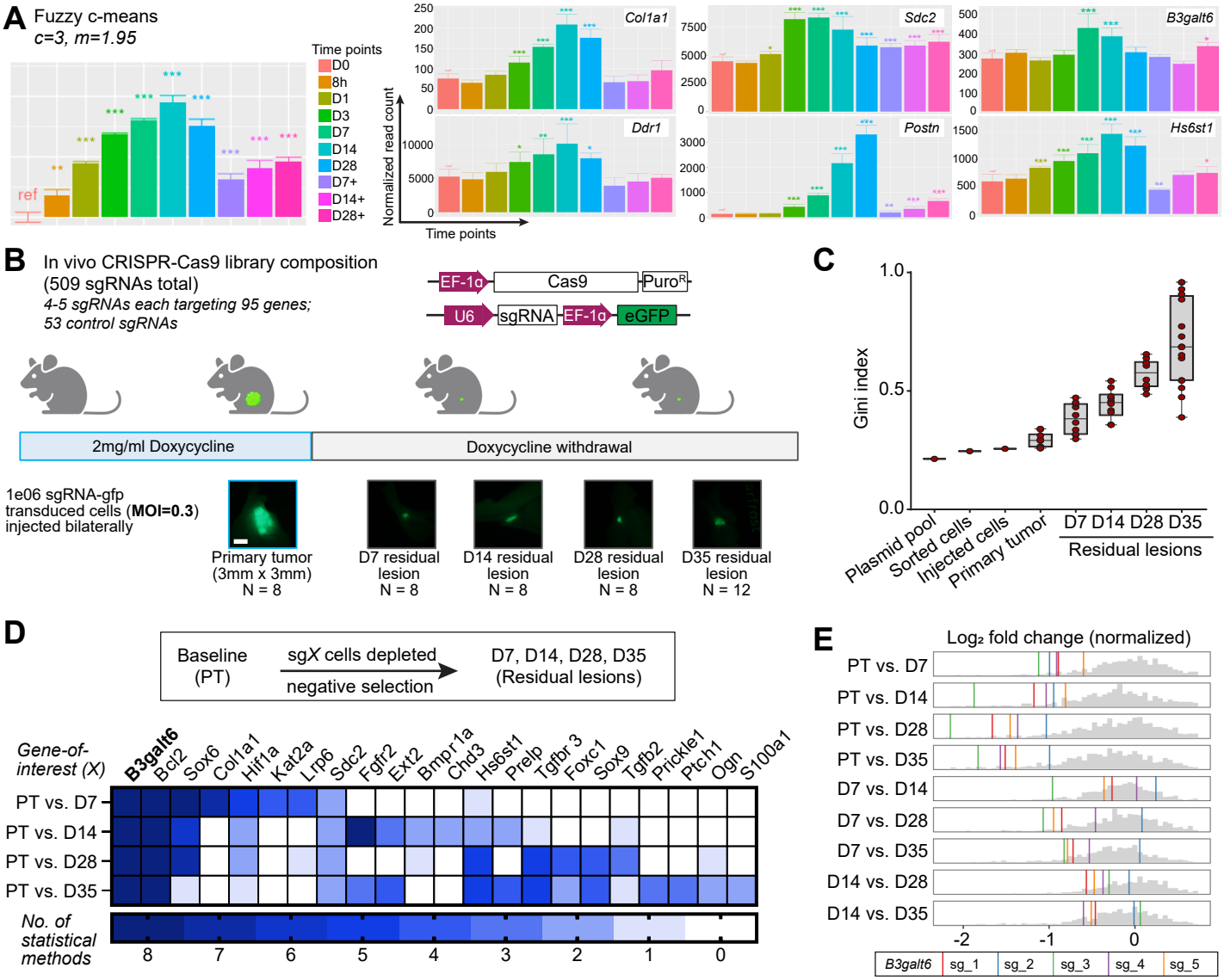

Fig. 2: An ECM-focused loss-of-function screen identifies *B3galt6* as a novel regulator of RTC fitness in vivo

A. Fuzzy c-means clustering using cluster # (c)=3, fuzzifier (m)=1.95 identifies one cluster that displays reversible, dormancy-dependent upregulation of genes at 8h, D1, D3, D7, D14, D28 (deinduction) time points. 6 genes (of 3450) in this cluster are indicated. Asterisks indicate significant changes in normalized read counts vs. D0 (baseline) *p<0.05, **p<0.01, ***p<0.001, ****p<0.001. **B.** In vivo CRISPR-Cas9 screen schematic. Stereoscope images of representative lesions are shown. Scale bar=2mm. **C.** Gini index for heterogeneity at sequential time points assayed in the screen. Data are represented as median ± range. **D.** Target identification criterion and list of CRISPR-Cas9 screen depletion hits identified by 2-8 statistical methods used for calling hits. **E.** Log_2 fold change (normalized) gene-level effect size plots for *B3galt6* sgRNAs in different pairwise comparisons using PT, D7, or D14 as baselines. Grey histogram depicts the background distribution of sgRNAs in the CRISPR-Cas9 screen, colored vertical lines depict each sgRNA targeting *B3galt6*.

bioRxiv preprint doi: https://doi.org/10.1101/2023.01.31.526529; this version posted February 3, 2023. The copyright holder for this preprint (which was not certified by peer review) is the author/funder, who has granted bioRxiv a license to display the preprint in perpetuity. It is made available under aCC-BY-NC-ND 4.0 International license.

Figure 3

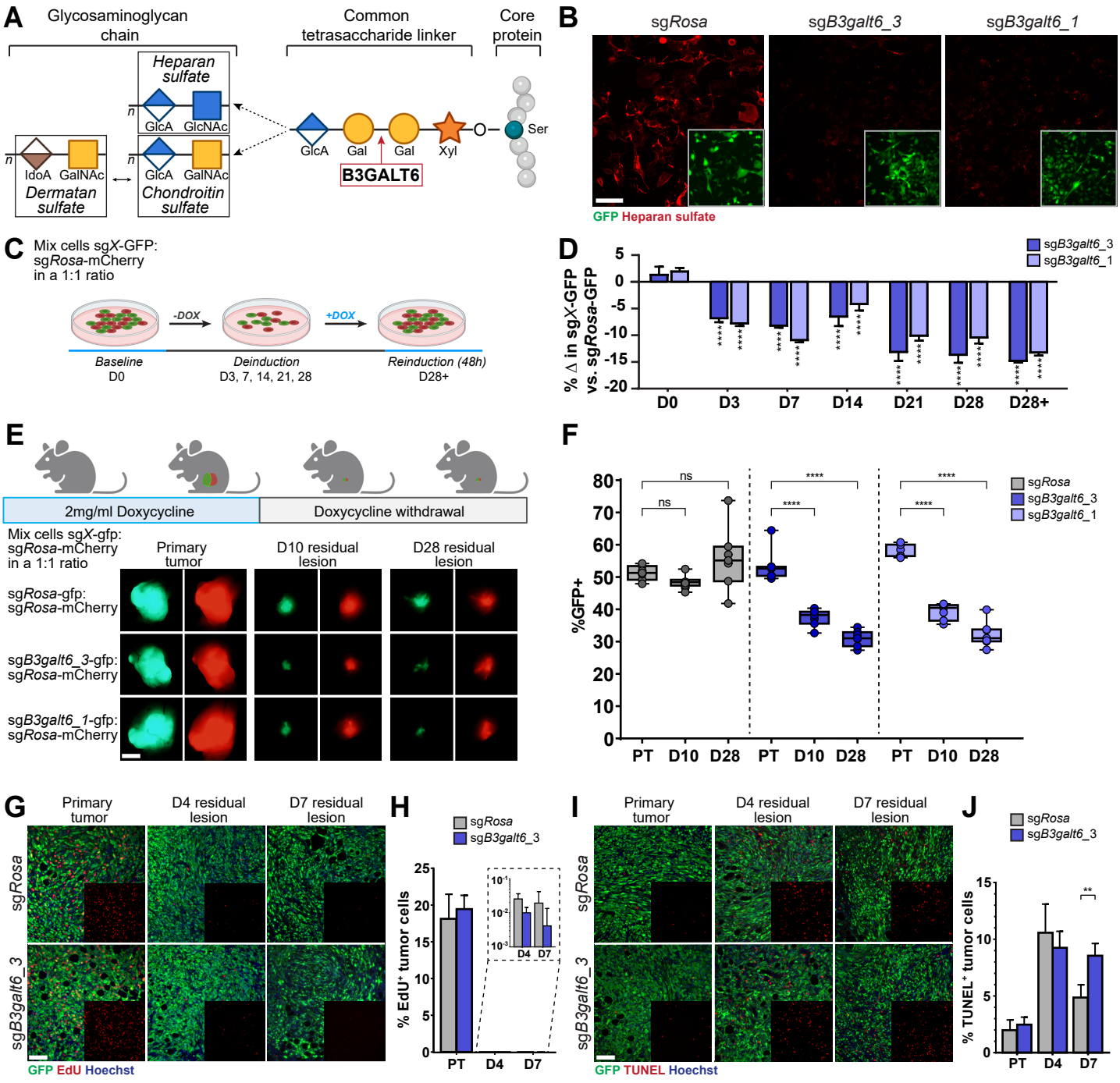

Fig. 3: B3GALT6 promotes RTC survival during dormancy

A. B3GALT6 (red box) function in tetrasaccharide linker synthesis and proteoglycan assembly. Typical disaccharide repeat units in heparan sulfate, chondroitin sulfate, and dermatan sulfate are indicated. Ser=Serine, Xyl=Xylose, Gal=Galactose, GlcA=Glucuronic acid, GlcNAc=N-Acetylglucosamine, GalNAc=N-Acetylgalactosamine, IdoA=Iduronic acid. **B.** Immunofluorescence for heparan sulfate (red) in Her2-dependent-Cas9 cells transduced with sg*Rosa*, sg*B3galt6*_3, or sg*B3galt6*_1 sgRNAs (green). Scale bar=100μm. **C.** IVD competition assay schematic. **D.** ddPCR data quantifying percentage change in sg*B3galt6_3* (dark blue) and sg*B3galt6*_1 (light blue) GFP+ cells normalized to sg*Rosa* (grey) cell numbers. Data are represented as mean ± SD. ****p<0.001. **E.** Schematic for in vivo competition assay with stereoscope images of representative lesions harvested. Scale bar=2mm. **F.** ddPCR data quantifying GFP+ cell percentage in sg*Rosa* (grey), sg*B3galt6*_3 (dark blue), and sg*B3galt6*_1 (light blue) groups. Data are represented as median ± range. ns=non-significant, ****p<0.001. **G-J.** Immunofluorescence (**G**) and quantification (**H**) for EdU (red) or for TUNEL (red) (**I, J**) in Her2-dependent-Cas9 sg*Rosa* and sg*B3galt6*_3 (green) PTs, D4, and D7 residual lesions (RLs). Scale bar=100μm. Quantification in the sg*Rosa* (grey) and sg*B3galt6*_3 (dark blue) groups is represented as mean ± SD. **p<0.01.

bioRxiv preprint doi: https://doi.org/10.1101/2023.01.31.526529; this version posted February 3, 2023. The copyright holder for this preprint (which was not certified by peer review) is the author/funder, who has granted bioRxiv a license to display the preprint in perpetuity. It is made available under aCC-BY-NC-ND 4.0 International license.

Figure 4

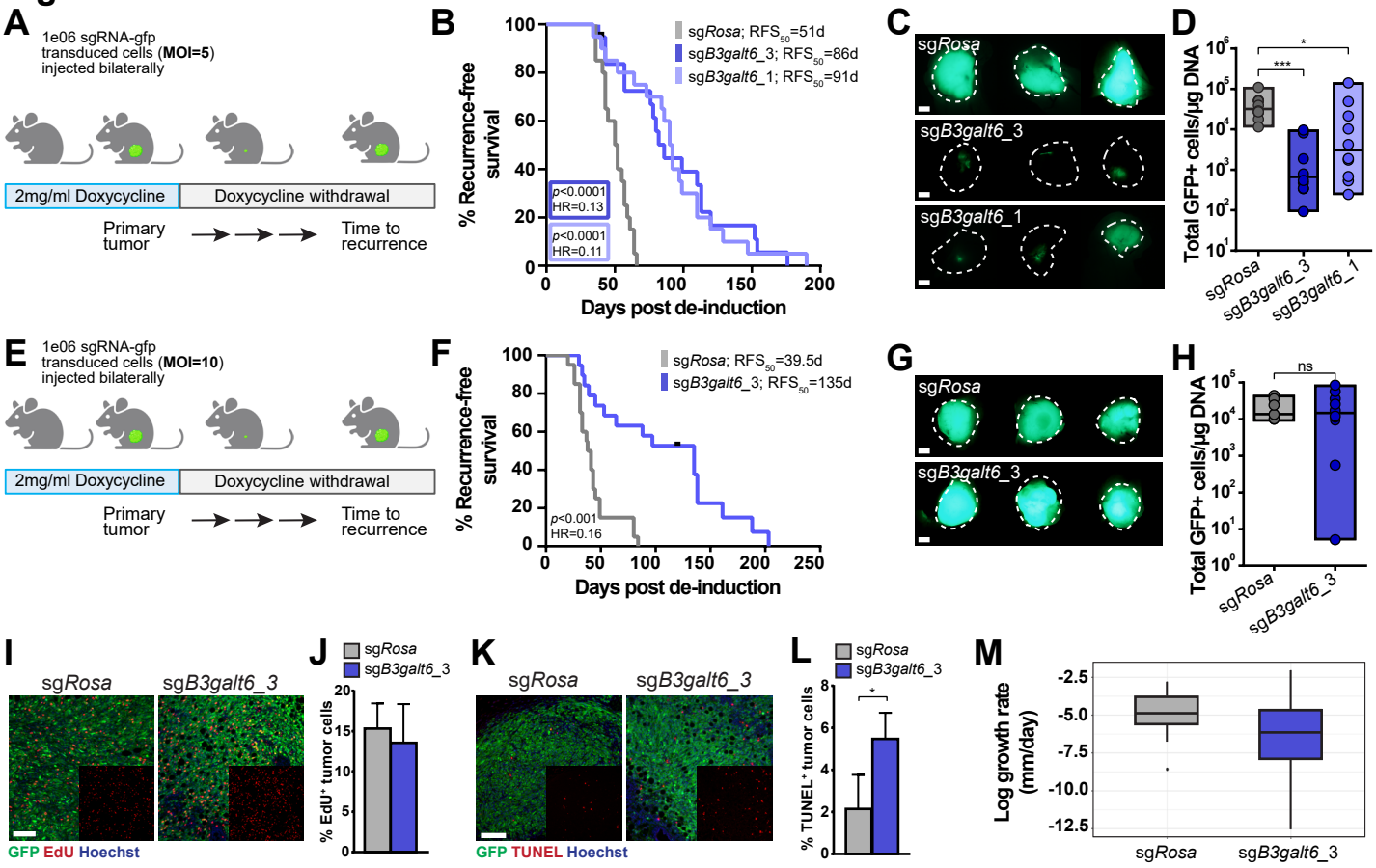

Fig. 4: B3GALT6 promotes recurrence following dormancy

A. Recurrence-free survival assay using multiplicity of infection (MOI)=5. **B.** Kaplan-Meier analysis of recurrence-free survival for sg*Rosa* (grey), sg*B3galt6*_3 (dark blue), and sg*B3galt6*_1 (light blue) groups. RFS_{50}=median time-to-recurrence. **C.** Stereoscope images of representative recurrences. Dotted white lines represent tumor edges identified in corresponding bright field images. Scale bar=2mm. **D.** Quantification of GFP+ cells in recurrent tumors as measured by ddPCR for sg*Rosa* (grey), sg*B3galt6*_3 (dark blue), and sg*B3galt6*_1 (light blue) groups. Data are represented as median ± range. **p*<0.05, ***p*<0.001. **E.** Recurrence-free survival assay using MOI=10. **F.** Kaplan-Meier analysis of recurrence-free survival for sg*Rosa* (grey) and sg*B3galt6*_3 (dark blue) groups. RFS_{50}=median time-to-recurrence. **G.** Stereoscope images of representative recurrences. Scale bar=2mm. **H.** Quantification of GFP+ cells measured by ddPCR for sg*Rosa* (grey) and sg*B3galt6*_3 (dark blue) recurrences. Data are represented as median ± range. ns=non-significant. **I-L.** Immunofluorescence (**I**) and quantification (**J**) for EdU (red) or for TUNEL (red) (**K, L**) in Her2-dependent-Cas9 sg*Rosa* and sg*B3galt6*_3 (green) recurrences. Scale bar=100µm. Quantification in sg*Rosa* (grey) and sg*B3galt6*_3 (dark blue) groups is represented as mean ± SD. **p*<0.05. **M.** Log growth rate of sg*Rosa* (grey) and sg*B3galt6*_3 (dark blue) recurrent tumors. Data are represented as median ± interquartile range.

bioRxiv preprint doi: https://doi.org/10.1101/2023.01.31.526529; this version posted February 3, 2023. The copyright holder for this preprint (which was not certified by peer review) is the author/funder, who has granted bioRxiv a license to display the preprint in perpetuity. It is made available under aCC-BY-NC-ND 4.0 International license.

Figure 5

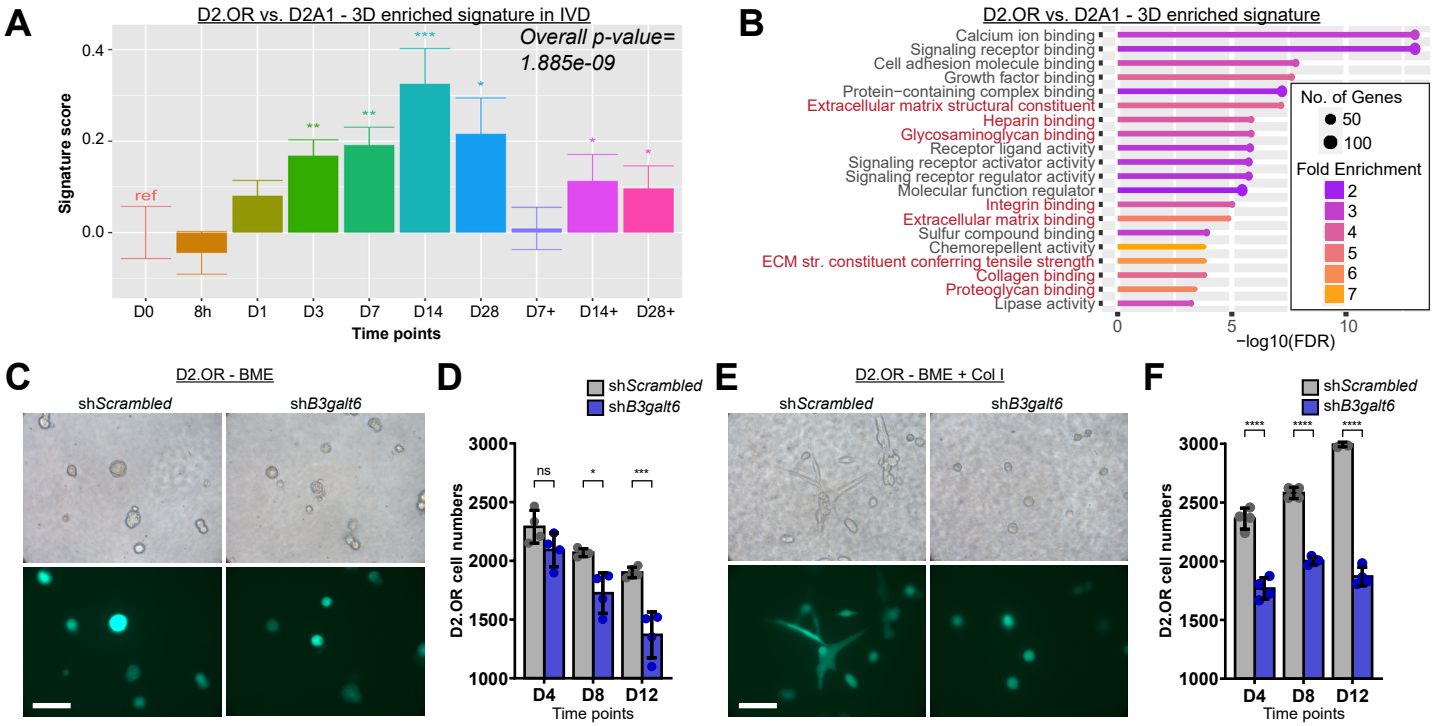

Fig. 5: B3GALT6 promotes tumor cell survival and outgrowth in microenvironment-induced models of dormancy
A. Application of a gene expression signature derived from D2.OR (indolent) cells vs. D2A1 (aggressive) cells in 3D to IVD temporal profiling of Her2-dependent tumor cells. Asterisks indicate significant changes in normalized read counts vs. D0 (*baseline*) **p*<0.05, ***p*<0.01, ****p*<0.001. **B.** Top 20 gene ontology terms for the overlapping upregulated set of 1018 genes. ECM-associated categories are highlighted in red. **C.** Brightfield and fluorescence images of sh*Scrambled* and sh*B3galt6* D2.OR cells grown in 3D on basement membrane extract (BME) and **D.** viable cell numbers measured at D4, D8, and D12 time points. Scale bar=100μm. Data are represented as mean ± SD. ns=non-significant, **p*<0.05, *****p*<0.0001. **E.** Brightfield and fluorescence images of sh*Scrambled* and sh*B3galt6* D2.OR cells grown in 3D on BME + Col I and **F.** viable cell numbers measured at D4, D8, and D12 time points. Scale bar=100μm. Data are represented as mean ± SD. ns=non-significant, **p*<0.05, *****p*<0.0001.

bioRxiv preprint doi: https://doi.org/10.1101/2023.01.31.526529; this version posted February 3, 2023. The copyright holder for this preprint (which was not certified by peer review) is the author/funder, who has granted bioRxiv a license to display the preprint in perpetuity. It is made available under aCC-BY-NC-ND 4.0 International license.

Figure 6

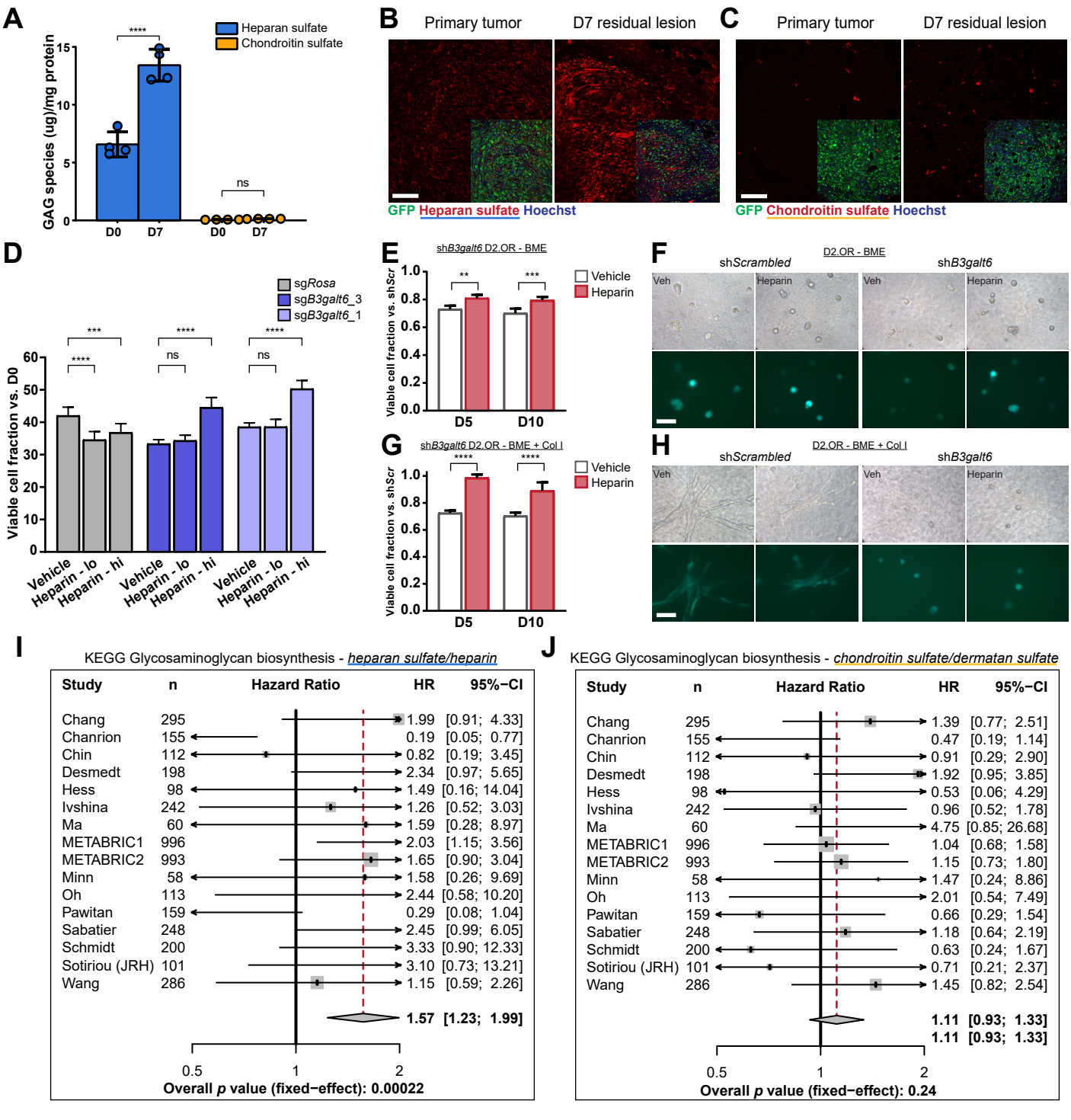

Fig. 6: Heparan sulfate synthesis is upregulated during dormancy and associated with worse recurrence-free survival in breast cancer patients

A. Liquid chromatography/mass spectrometry (LC/MS) analysis of heparan sulfate (blue) and chondroitin sulfate (yellow) GAGs performed on D0 and D7 in vitro samples. Data are represented as mean ± SD. ns=non-significant, ****p<0.0001. **B.** Immunofluorescence for heparan sulfate or **C.** chondroitin sulfate (right panels) (red) in PTs and D7 RLs derived from Her2-dependent-Cas9 cells with sg*Rosa* (green). Scale bar=100μm. **D.** Viable cell numbers measured at D7 following daily treatment of Her2-dependent cells with vehicle, heparin low dose (lo; 5μg/ml), or heparin high dose (hi; 25μg/ml). ns=non-significant, ***p<0.001, ****p<0.001. **E.** Viable shB3galt6 cell numbers normalized to shScrambled controls measured at D5 and D10 following treatment of D2.OR cells in BME with vehicle (grey) or heparin (25μg/ml, red) and **F.** fluorescence images. **p<0.01, ***p<0.001. Scale bar=100μm. **G.** Viable shB3galt6 cell numbers normalized to shScrambled controls measured at D5 and D10 following treatment of D2.OR cells in BME + Col I with vehicle (grey) or heparin (25μg/ml, red) and **H.** fluorescence images. Scale bar=100μm. ****p<0.0001. **I.** Forest plots of hazard ratios (HR) and 95% confidence intervals (CI) as a function of heparan sulfate/heparin or **J.** chondroitin sulfate/der-

bioRxiv preprint doi: https://doi.org/10.1101/2023.01.31.526529; this version posted February 3, 2023. The copyright holder for this preprint (which was not certified by peer review) is the author/funder, who has granted bioRxiv a license to display the preprint in perpetuity. It is made available under aCC-BY-NC-ND 4.0 International license.

matan sulfate KEGG biosynthesis signatures in breast cancer patients recurring within 10 years after initial treatment. Red dashed lines depict the shift in HR across 16 human datasets.

bioRxiv preprint doi: https://doi.org/10.1101/2023.01.31.526529; this version posted February 3, 2023. The copyright holder for this preprint (which was not certified by peer review) is the author/funder, who has granted bioRxiv a license to display the preprint in perpetuity. It is made available under aCC-BY-NC-ND 4.0 International license.

Figure 7

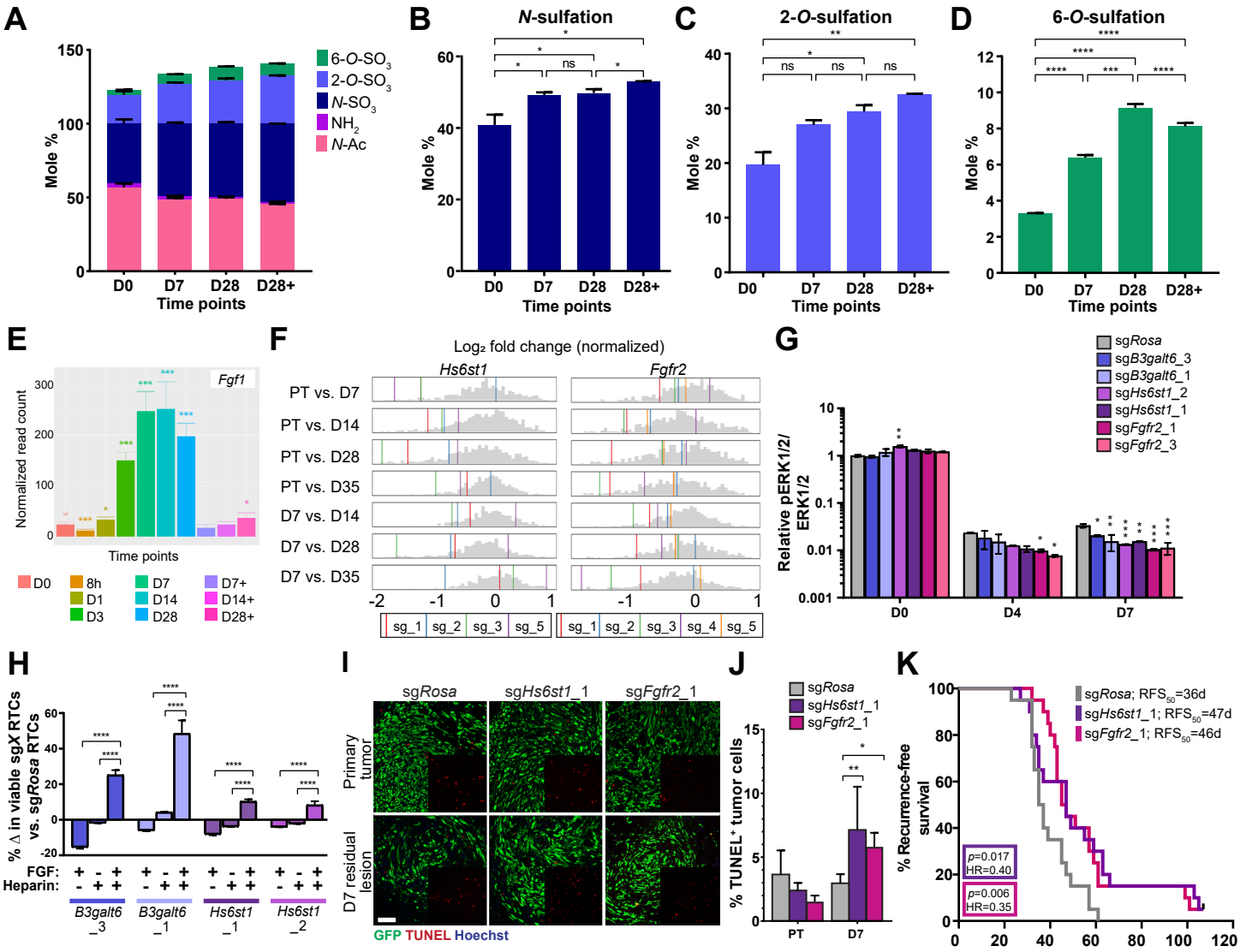

Fig. 7: Heparan sulfate 6-*O*-sulfation is selectively upregulated during dormancy and promotes RTC survival by potentiating FGF1 signaling

A. LC/MS on D0 (*baseline*), D7, D28 (*deinduction*), and D28+ (*reinduction*) IVD samples identifying the molar percentages of modifications on disaccharide units comprising iduronic/glucuronic acid and glucosamine. Relative proportions of N-acetylglucosamine (N-Ac; light pink), unsubstituted glucosamine (NH_2; dark pink), **B.** N-sulfoglucosamine (N-S; dark blue), **C.** Uronyl-2-*O*-sulfates (2-*O*-SO_3; light blue), and **D.** Glucosaminyl-6-*O*-sulfates (6-*O*-SO_3; green) are depicted as mean ± SD. ns=non-significant, **p*<0.05, ***p*<0.01, ****p*<0.001, *****p*<0.001. **E.** Normalized read counts indicating reversible upregulation of *Fgf1* at 8h, D1, D3, D7, D14, D28 (*deinduction*) time points. Asterisks indicate significant changes in normalized read counts vs. D0 (*baseline*) **p*<0.05, ****p*<0.001. **F.** Log_2 fold-change (normalized) gene-level effect size plots for *B3galt6* in pairwise comparisons using PT or D7 as baselines. Grey histogram depicts the background distribution of sgRNAs in the CRISPR-Cas9 screen, colored vertical lines depict each sgRNA targeting *Hs6st1* or *Fgfr2*. **G.** Western blot analysis of phospho-ERK1/2 (pERK1/2) and total ERK1/2 (tERK1/2) levels in sg*Rosa*, sg*B3galt6*_3, sg*B3galt6*_1, sg*Hs6st1*_2, sg*Hs6st1*_1, sg*Fgfr2*_2, and sg*Fgfr2*_3 Her2-dependent-Cas9 cells at D0 (*baseline*), D4, and D7 (*deinduction*) time points. Numbers indicate relative quantification of pERK1/2/tERK1/2 signal normalized to sgRosa levels within each time point. **H.** Viable RTC counts at D7 quantifying the percentage change relative to sgRosa RTCs in sg*B3galt6*_3, sg*B3galt6*_1, sg*Hs6st1*_2, and sg*Hs6st1*_1 Her2-dependent-Cas9 cells treated with FGF1 (25ng/ml), heparin (25µg/ml), or FGF1 (25ng/ml) + heparin (25µg/ml). *****p*<0.0001. **I.** Immunofluorescence and **J.** quantification for TUNEL (red) in Her2-dependent-Cas9 sg*Rosa*, sg*Hs6st1*_1, and sg*Fgfr2*_1 (green) PTs and D7 RLs. Scale bar=100µm. Quantification in the sg*Rosa* (grey), sg*Hs6st1*_1 (purple), and sg*Fgfr2*_1 (pink) groups is represented as mean ± SD. **p*<0.05, ***p*<0.01. **K.** Kaplan-Meier analysis of recurrence-free survival for the sg*Rosa* (grey), sg*Hs6st1*_1 (purple), and sg*Fgfr2*_1 (pink) groups. RFS_{50}=median time-to-recurrence.

bioRxiv preprint doi: https://doi.org/10.1101/2023.01.31.526529; this version posted February 3, 2023. The copyright holder for this preprint (which was not certified by peer review) is the author/funder, who has granted bioRxiv a license to display the preprint in perpetuity. It is made available under aCC-BY-NC-ND 4.0 International license.

Figure S1

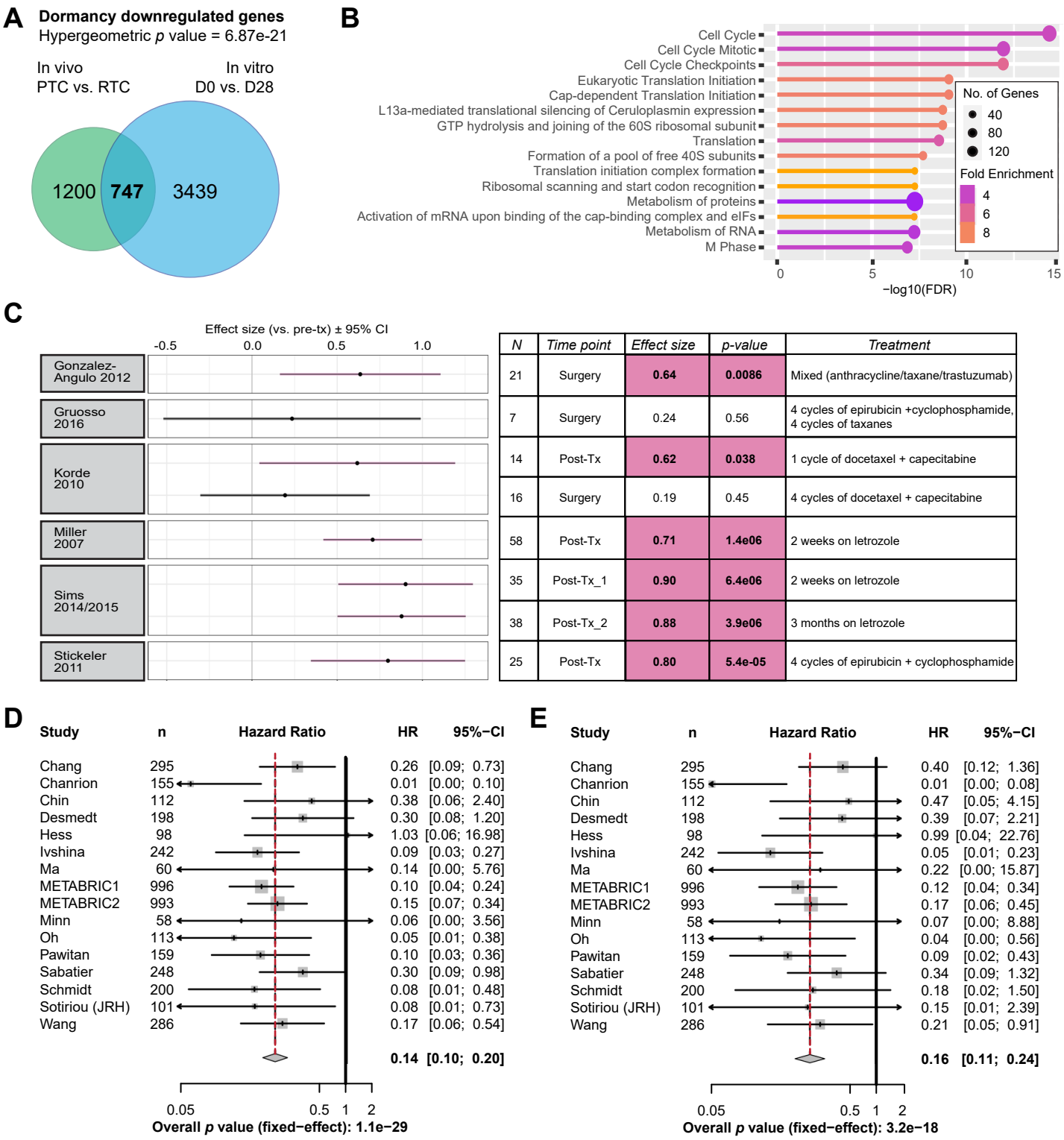

N	Time point	Effect size	p-value	Treatment
21	Surgery	**0.64**	**0.0086**	Mixed (anthracycline/taxane/trastuzumab)
7	Surgery	0.24	0.56	4 cycles of epirubicin +cyclophosphamide, 4 cycles of taxanes
14	Post-Tx	**0.62**	**0.038**	1 cycle of docetaxel + capecitabine
16	Surgery	0.19	0.45	4 cycles of docetaxel + capecitabine
58	Post-Tx	**0.71**	**1.4e06**	2 weeks on letrozole
35	Post-Tx_1	**0.90**	**6.4e06**	2 weeks on letrozole
38	Post-Tx_2	**0.88**	**3.9e06**	3 months on letrozole
25	Post-Tx	**0.80**	**5.4e-05**	4 cycles of epirubicin + cyclophosphamide

Fig. S1: A. Hypergeometric test and Venn diagram depicting the overlap between the in vivo and IVD-derived downregulated gene set. **B.** Top 15 Reactome gene ontology terms for the overlapping upregulated set of 747 genes is depicted on the bar plot. **C.** Dormancy-associated tumor cell-autonomous gene signature (after subtracting out genes that belong to the gene ontology term 'Cell Cycle') enrichment following neoadjuvant therapies vs. pre-treatment (pre-tx) samples across 7 different datasets is measured by effect size. Significant effects are highlighted in pink. **D.** Forest plot representation of hazard ratios (HR) and 95% confidence intervals (CI) as a function of the dormancy-signature or **E.** dormancy signature after subtracting out genes that belong to the gene ontology term 'Cell Cycle' in breast cancer patients recurring 10 years after initial treatment. Red dashed lines depict the shift in HR across 16 human datasets. Forest plot representation of hazard ratios (HR) and 95% confidence intervals (CI) as a function of the dormancy-signature in breast cancer patients recurring 10 years after initial treatment.

bioRxiv preprint doi: https://doi.org/10.1101/2023.01.31.526529; this version posted February 3, 2023. The copyright holder for this preprint (which was not certified by peer review) is the author/funder, who has granted bioRxiv a license to display the preprint in perpetuity. It is made available under aCC-BY-NC-ND 4.0 International license.

Figure S2

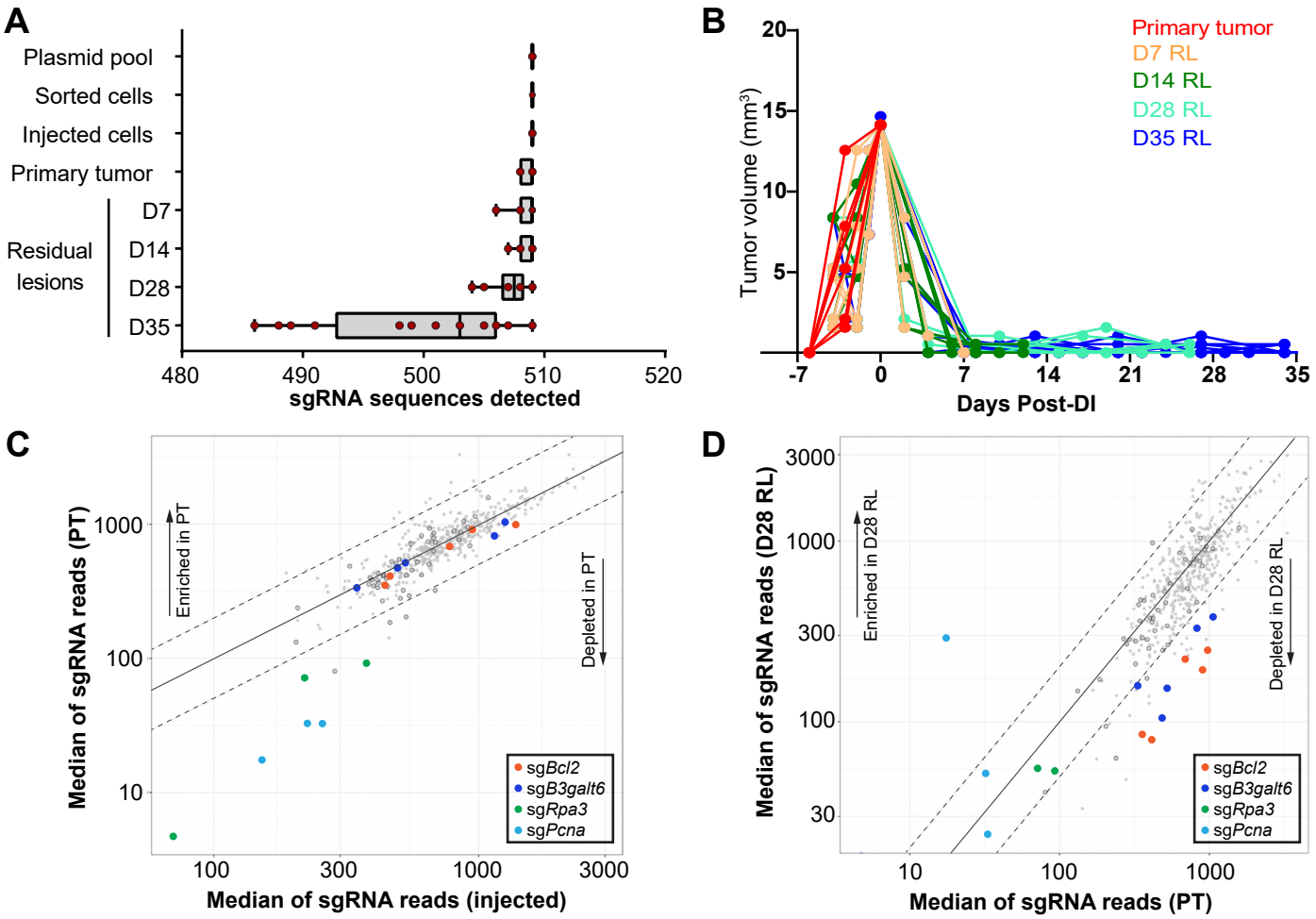

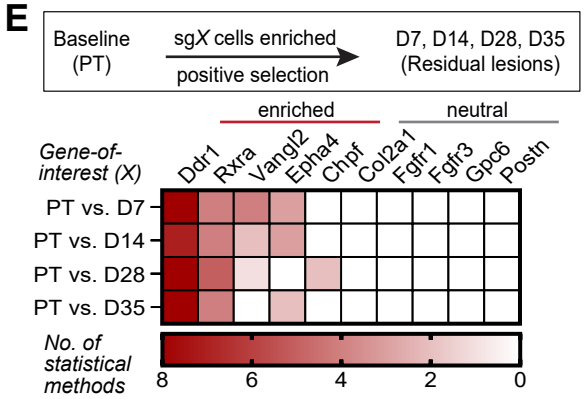

F

B3galt6

Method	PT_D7	PT_D14	PT_D28	PT_D35	D7_D14	D7_D28	D7_D35	D14_D28	D14_D35
MAGeCK-RRA-M	-4.82	-3.55	-4.46	-3.52	-0.90	-1.24	-0.29	-0.55	-0.33
MAGeCK-RRA-T	-5.30	-3.55	-4.60	-2.00	-0.47	-1.14	-0.43	-1.64	-0.25
MW-RRA-MoR	-2.59	-3.26	-4.08	-3.48	0.00	-1.80	-1.57	-1.54	-0.65
MW-RRA-NC_MoR	-2.87	-2.82	-4.20	-3.31	0.00	-2.07	-1.67	-1.96	-0.53
MW-RRA-NC_RZ	-1.60	-2.10	-2.27	-2.75	0.00	-0.58	0.00	-0.37	0.35
MW-RRA-NR	-2.00	-1.70	-3.43	-1.95	0.00	-1.02	0.13	-0.51	0.03
MW-RRA-RZ	-1.67	-1.71	-4.08	-1.89	0.00	-1.17	0.00	-0.92	0.00
MW-RRA-TMM	-3.01	-3.79	-4.57	-3.73	0.00	-2.31	-1.95	-1.51	-0.83

Fig. S2: A. Number of sgRNAs (out of 509) detected in every sample at sequential time points in the CRISPR-Cas9 screen. Data are represented as median ± interquartile range. **B.** Palpation data tracking tumor volumes for all harvested samples at PT and RL time points. **C, D** Scatterplot of sgRNA sequence reads normalized by MoR in injected vs. PT samples (**C**) and PT vs. D28 RL (**D**). Solid line indicates identity line, dotted lines indicate two-fold differences. Outlined grey circles indicate non-targeting sgRNAs. **E.** Subset of CRISPR-Cas9 screen enrichment hits (5 genes) identified by 2-8 statistical methods (MAGeCK-RRA-M, MAGeCK-RRA-T, MW-RRA-MoR, MW-RRA-NC_MoR, MW-RRA-NC_RZ, MW-RRA-NR, MW-RRA-RZ, MW-RRA-TMM) and neutral genes (5 genes) displaying no selection during dormancy. **F.** Scores indicate $-\log_{10}$(p value) for each pairwise comparison using PT, D7, or D14 as a baseline. Rows represent the statistical method being used. Positive values indicate enrichment of sgRNAs, negative values indicate depletion of sgRNAs. Significant results are highlighted in green.

bioRxiv preprint doi: https://doi.org/10.1101/2023.01.31.526529; this version posted February 3, 2023. The copyright holder for this preprint (which was not certified by peer review) is the author/funder, who has granted bioRxiv a license to display the preprint in perpetuity. It is made available under aCC-BY-NC-ND 4.0 International license.

Figure S3

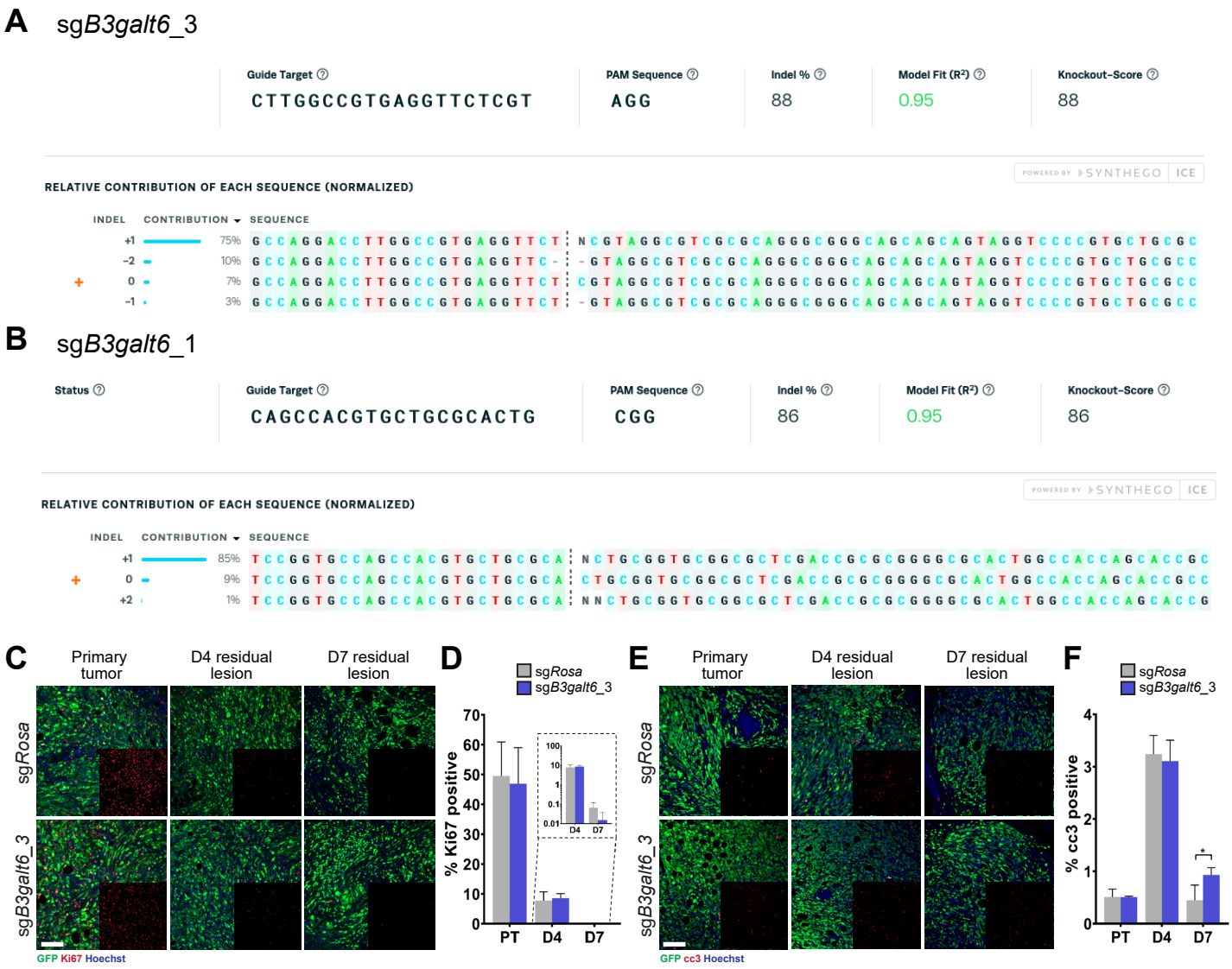

Fig. S3: A. Inference of CRISPR edits (ICE) analysis for sg*B3galt6*_3 and **B.** sg*B3galt6*_1 displaying the proportion of indels in the population. Wild-type sequence is represented by the orange + sign at 0. Dotted line indicates the Cas9 cut site. **C.** Immunofluorescence and **D.** associated quantification for Ki67 (red) or **E, F.** cleaved caspase 3 (cc3, red) in Her2-dependent-Cas9 sg*Rosa* and sg*B3galt6*_3 (green) PTs, D4, and D7 RLs. Scale bar=100μm. Quantification in the sg*Rosa* (grey) and sg*B3galt6*_3 (dark blue) groups is represented as mean ± SD. *p<0.05.

bioRxiv preprint doi: https://doi.org/10.1101/2023.01.31.526529; this version posted February 3, 2023. The copyright holder for this preprint (which was not certified by peer review) is the author/funder, who has granted bioRxiv a license to display the preprint in perpetuity. It is made available under aCC-BY-NC-ND 4.0 International license.

Figure S4

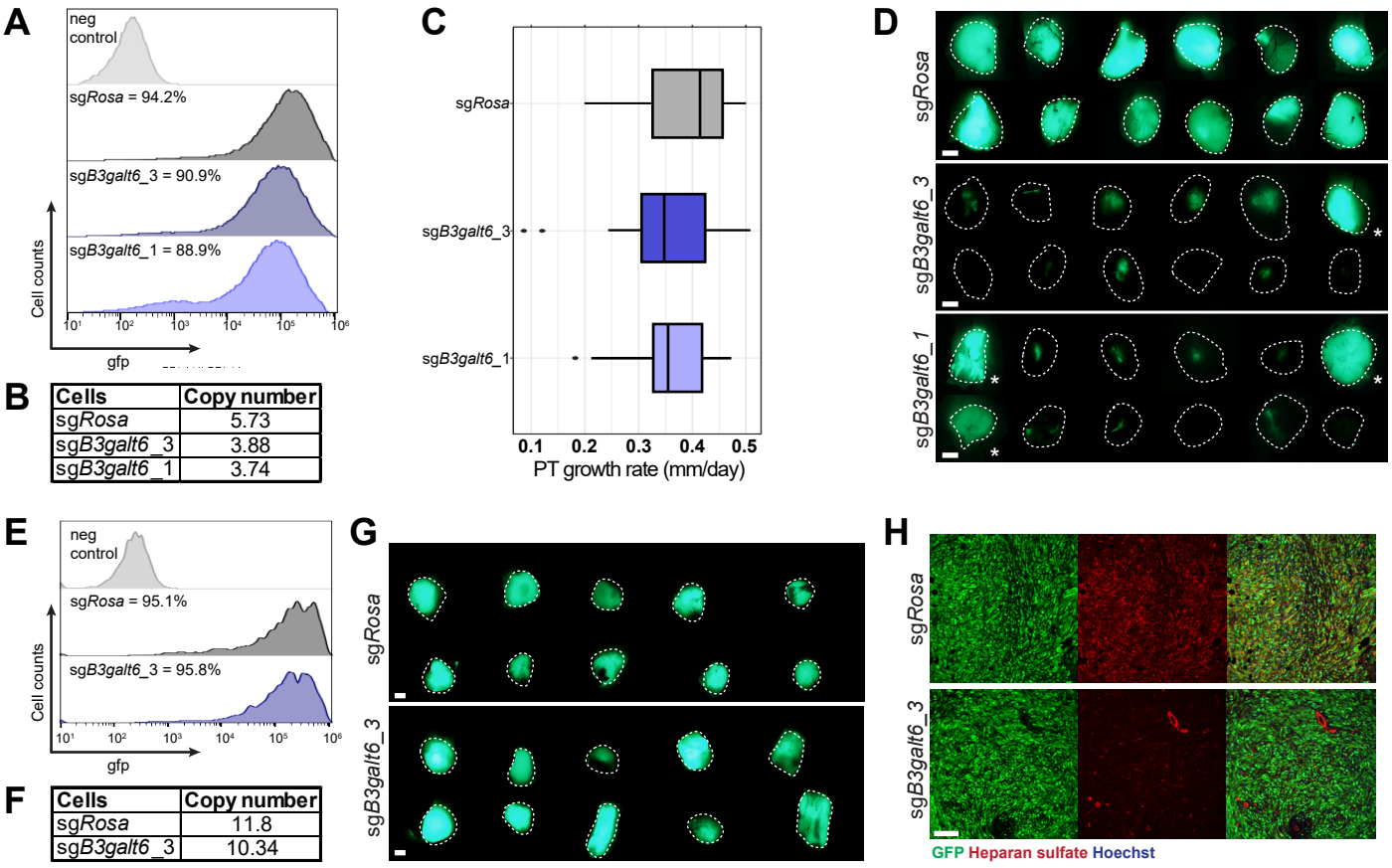

Cells	Copy number
sg*Rosa*	5.73
sg*B3galt6*_3	3.88
sg*B3galt6*_1	3.74

Cells	Copy number
sg*Rosa*	11.8
sg*B3galt6*_3	10.34

Fig. S4: A. Histograms represent the distribution of GFP positivity in the injected Her2-dependent-Cas9 sg*Rosa* (dark grey), sg*B3galt6*_3 (dark blue), and sg*B3galt6*_1 (light blue) relative to untransduced Her2-dependent-Cas9 cells (light grey). **B.** Average copy number of integrated GFP in the injected Her2-dependent-Cas9 sg*Rosa*, sg*B3galt6*_3, and sg*B3galt6*_1 cells detected by ddPCR. **C.** Growth rate of primary sg*Rosa* (dark grey), sg*B3galt6*_3 (dark blue), and sg*B3galt6*_1 (light blue) tumors. Data are represented as median ± interquartile range. **D.** Stereoscope images of 12 representative recurrences harvested. Dotted white lines drawn based on discernible tumor edges in bright field images. White asterisks indicate GFP+ recurrences in the sg*B3galt6*_3 and sg*B3galt6*_1 groups. Scale bar=2mm. **E.** Histograms represent the distribution of GFP positivity in the injected Her2-dependent-Cas9 sg*Rosa* (dark grey) and sg*B3galt6*_3 (dark blue) relative to untransduced Her2-dependent-Cas9 cells (light grey). **F.** Average copy number of integrated GFP in the injected Her2-dependent-Cas9 sg*Rosa* and sg*B3galt6*_3 cells detected by ddPCR. **G.** Stereoscope images of 10 representative recurrences harvested. Dotted white lines drawn based on discernible tumor edges in bright field images. Scale bar=2mm. **H.** Immunofluorescence for heparan sulfate (red) in Her2-dependent-Cas9 sg*Rosa* or sg*B3galt6*_3 (green) recurrences. Scale bar=100µm.

bioRxiv preprint doi: https://doi.org/10.1101/2023.01.31.526529; this version posted February 3, 2023. The copyright holder for this preprint (which was not certified by peer review) is the author/funder, who has granted bioRxiv a license to display the preprint in perpetuity. It is made available under aCC-BY-NC-ND 4.0 International license.

Figure S5

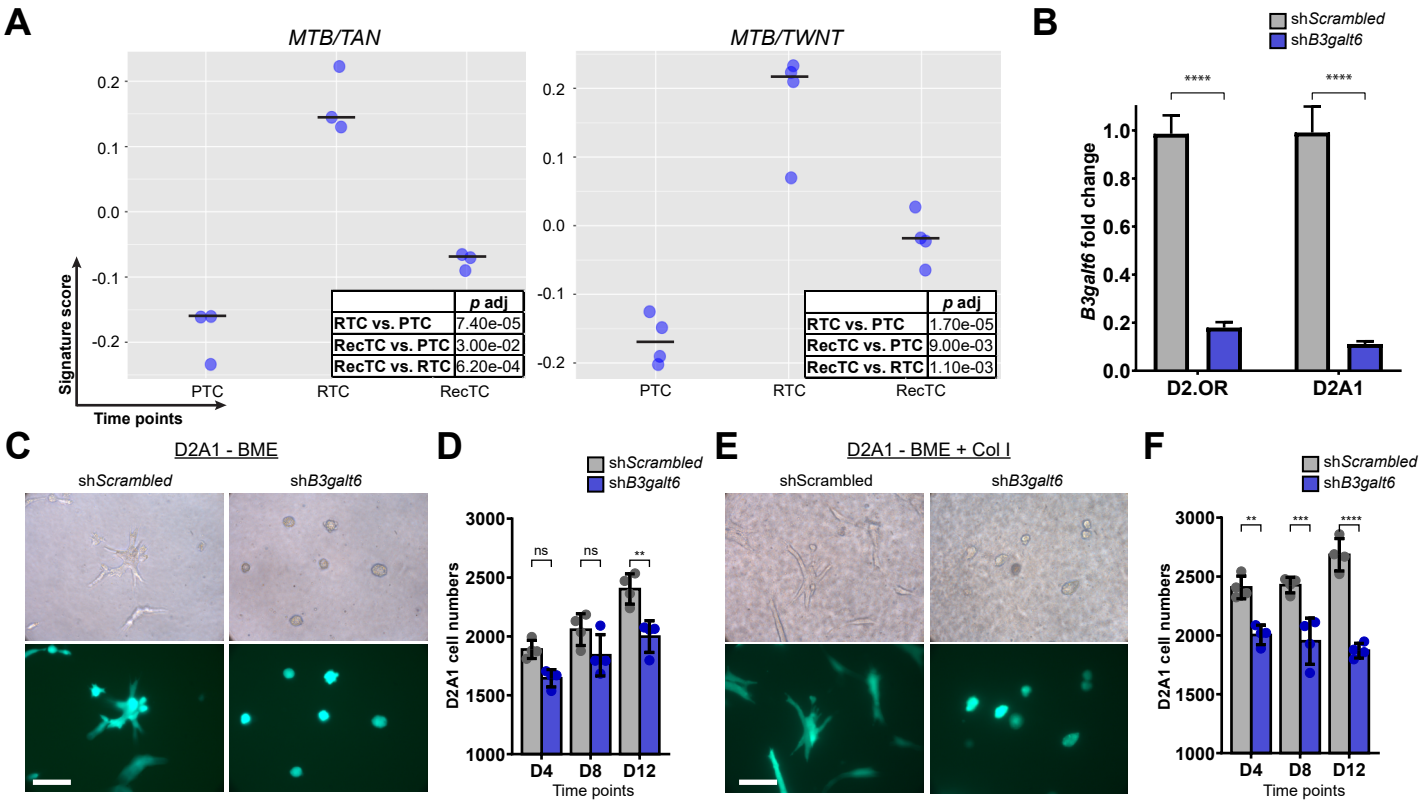

Fig. S5: A. Application of the gene expression signature derived from D2.OR (dormant, indolent) cells vs. D2A1 (proliferative, aggressive) cells in 3D to the *MTB/TAN* or *MTB/TWNT*-derived in vivo dormancy temporal profiling. Table represents adjusted *p* value for each pairwise comparison between primary tumor cells (PTC), residual tumor cells (RTC), and recurrent tumor cells (RecTC). Black lines indicate median score for each time point. **B.** qRT-PCR for *B3galt6* transcripts in sh*Scrambled* or sh*B3galt6* D2.OR and D2A1 cells. **C.** Brightfield and fluorescence images of sh*Scrambled* and sh*B3galt6* D2A1 cells grown in 3D on basement membrane extract (BME) and **D.** associated viable cell numbers measured by absorbance at 570nm at D0, D8, and D12 time points. Scale bar=100µm. Data are represented as mean ± SD. ns=non-significant, ***p*<0.01. **E.** Brightfield and fluorescence images of sh*Scrambled* and sh*B3galt6* D2A1 cells grown in 3D on BME + Col I and **F.** associated viable cell numbers measured by absorbance at 570nm at D0, D8, and D12 time points. Scale bar=100µm. Data are represented as mean ± SD. ***p*<0.01, ****p*<0.001, *****p*<0.0001.

bioRxiv preprint doi: https://doi.org/10.1101/2023.01.31.526529; this version posted February 3, 2023. The copyright holder for this preprint (which was not certified by peer review) is the author/funder, who has granted bioRxiv a license to display the preprint in perpetuity. It is made available under aCC-BY-NC-ND 4.0 International license.

Figure S6

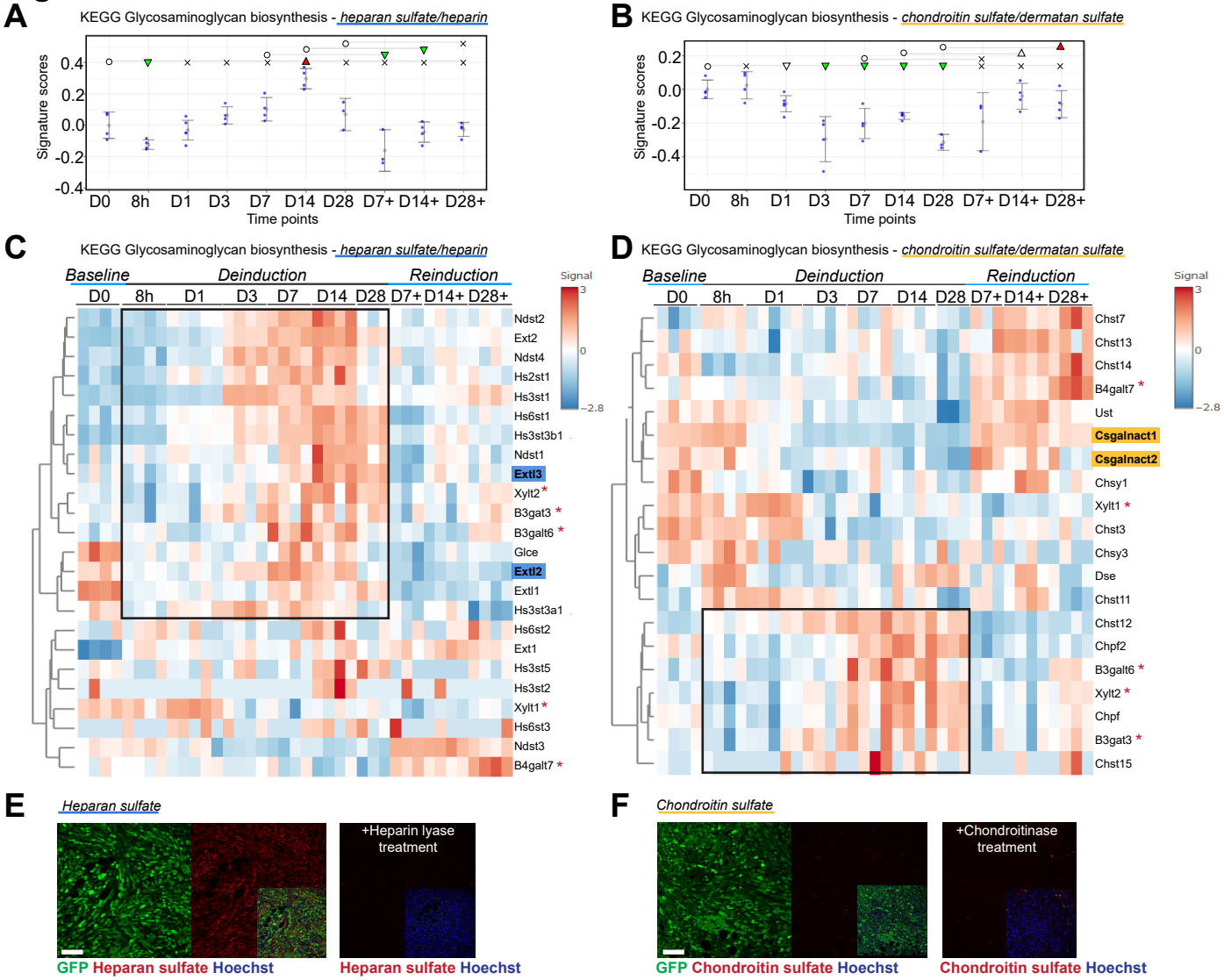

Fig. S6: A. Application of KEGG glycosaminoglycan (GAG) biosynthesis signatures for heparan sulfate/heparin and **B.** chondroitin sulfate/dermatan sulfate on MTB/TAN IVD temporal gene expression profiles. Circle=baseline, x=non-significant, empty triangles=trending significance 0.05<*p*<0.1, filled triangles=*p*<0.05, inverted triangles=decreased signature score, upright triangles=increased signature score. **C.** Heatmap of KEGG glycosaminoglycan (GAG) biosynthesis gene expression signatures for heparan sulfate/heparin (left) and **D.** chondroitin sulfate/dermatan sulfate (right) on *MTB/TAN* IVD temporal gene expression profiles. Black box represents the major group demonstrating dormancy-selective upregulation identified by hierarchical clustering. Red asterisks represent enzymes involved in tetrasaccharide linker synthesis during proteoglycan assembly. Blue boxes indicate enzymes involved in determining heparan sulfate synthesis, yellow boxes indicate enzymes involved in chondroitin sulfate synthesis. **E.** Immunofluorescence for heparan sulfate (left panels) or **F.** chondroitin sulfate (right panels) (red) in PTs derived from Her2-dependent-Cas9 cells with sg*Rosa* (green). Heparan sulfate/Chondroitin sulfate staining following heparin lyase or chondroitinase treatment is used as the negative control. Scale bar=100μm.

bioRxiv preprint doi: https://doi.org/10.1101/2023.01.31.526529; this version posted February 3, 2023. The copyright holder for this preprint (which was not certified by peer review) is the author/funder, who has granted bioRxiv a license to display the preprint in perpetuity. It is made available under aCC-BY-NC-ND 4.0 International license.

Figure S7

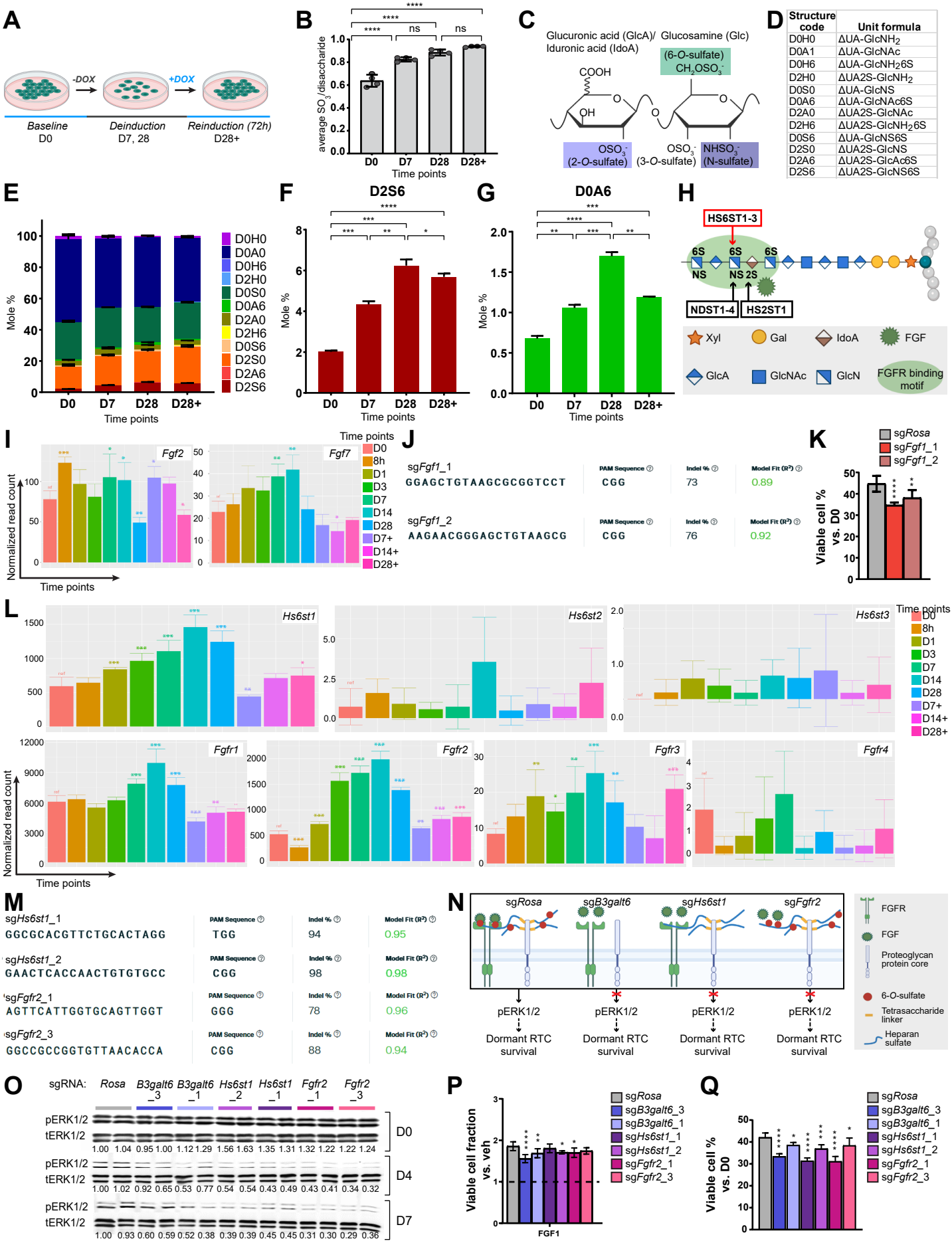

bioRxiv preprint doi: https://doi.org/10.1101/2023.01.31.526529; this version posted February 3, 2023. The copyright holder for this preprint (which was not certified by peer review) is the author/funder, who has granted bioRxiv a license to display the preprint in perpetuity. It is made available under aCC-BY-NC-ND 4.0 International license.

Fig. S7: A. Experimental setup for IVD samples isolated for LC/MS for heparan sulfate and chondroitin sulfate disaccharide analysis. **B.** Average sulfation/disaccharide of heparan sulfate at D0 (*baseline*), D7, D28 (*deinduction*), and D28+ (*reinduction*) time points measured by LC/MS. Data are represented as mean ± SD. ns=non-significant, ****p<0.0001. **C.** Possible sites of sulfation on the heparan sulfate disaccharide. Colored boxes indicate the types of sulfation assessed. **D.** 4-character disaccharide structure code (DSC) nomenclature and unit formulae. ΔUA – Δ4,5-unsaturated uronic acid. **E.** Distribution of heparan sulfate disaccharide motifs at IVD time points represented according to the 4-character disaccharide structure code (DSC) nomenclature. Molar percentages of (**F**) D2S6 and (**G**) D0A6 are highlighted. Data are represented as mean ± SD. ns=non-significant, *p<0.05, **p<0.01, ***p<0.001, ****p<0.0001. **H.** Pictorial representation of the substrates and the type of sulfation catalyzed by sulfotransferase enzymes to generate protein binding motifs, *e.g.*, FGFR binding motif. **I.** Normalized read counts indicating the expression of *Fgf2* and *Fgf7*. Asterisks indicate significant changes in normalized read counts vs. D0 (*baseline*) *p<0.05, ** p<0.01. **J.** Inference of CRISPR edits (ICE) analysis for sg*Fgf1*_1 and sg*Fgf1*_2 displaying the proportion of indels in the population. **K.** Viable RTC counts relative to D0 in sg*Rosa*, sg*Fgf1*_1, and sg*Fgf1*_2 Her2-dependent-Cas9 cells. **p<0.01, ****p<0.0001. **L.** Normalized read counts indicating the expression of *Hs6st1-3* and *Fgfr1-4*. Asterisks indicate significant changes in normalized read counts vs. to D0 (*baseline*) *p<0.05, **p<0.01, ***p<0.001. **M.** Inference of CRISPR edits (ICE) analysis for sg*Hs6st1*_1, sg*Hs6st1*_2, sg*Fgfr2*_1, sg*Fgfr2*_3 displaying the proportion of indels in the population. **N.** Schematic depicting the role of heparan sulfate, 6-*O*-sulfation, and FGF signaling in maintain dormant RTC survival. **O.** Western blot quantification of phospho-ERK1/2 (pERK1/2) over total ERK1/2 (tERK1/2) levels in sg*Rosa*, sg*B3galt6*_3, sg*B3galt6*_1, sg*Hs6st1*_2, sg*Hs6st1*_1, sg*Fgfr2*_2, and sg*Fgfr2*_3 Her2-dependent-Cas9 cells at D0 (*baseline*), D4, and D7 (*deinduction*) time points. pERK1/2/tERK1/2 signal normalized to sg*Rosa* levels at D0. Asterisks indicate significant changes vs. sg*Rosa* signal within the time point (*baseline*) *p<0.05, **p<0.01, ***p<0.001. **P.** Viable RTC counts relative to vehicle-treated cells (black dashed line) at D4 in sg*Rosa*, sg*B3galt6*_3, sg*B3galt6*_1, sg*Hs6st1*_2, sg*Hs6st1*_1, sg*Fgfr2*_1, and sg*Fgfr2*_3 Her2-dependent-Cas9 cells treated with FGF1 (25ng/ml). Black dotted line indicates the viable cell number in the vehicle controls. *p<0.05, **p<0.01, ****p<0.0001. **Q.** Viable RTC counts relative to D0 in sg*Rosa*, sg*B3galt6*_3, sg*B3galt6*_1, sg*Hs6st1*_2, sg*Hs6st1*_1, sg*Fgfr2*_1, and sg*Fgfr2*_3 Her2-dependent-Cas9 cells. *p<0.05, ****p<0.0001.